

2009

Accurate determination of nonlinear optical parameters of semiconductors at infrared wavelengths

Leonel Pastor Gonzalez
University of Dayton

Follow this and additional works at: https://ecommons.udayton.edu/graduate_theses

Recommended Citation

Gonzalez, Leonel Pastor, "Accurate determination of nonlinear optical parameters of semiconductors at infrared wavelengths" (2009). *Graduate Theses and Dissertations*. 2945.
https://ecommons.udayton.edu/graduate_theses/2945

This Dissertation is brought to you for free and open access by the Theses and Dissertations at eCommons. It has been accepted for inclusion in Graduate Theses and Dissertations by an authorized administrator of eCommons. For more information, please contact mschlange1@udayton.edu, ecommons@udayton.edu.

ACCURATE DETERMINATION OF NONLINEAR OPTICAL
PARAMETERS OF SEMICONDUCTORS AT INFRARED
WAVELENGTHS

Dissertation

Submitted to

The School of Engineering of the

UNIVERSITY OF DAYTON

In Partial Fulfillment of the Requirements for

The Degree

Doctor of Philosophy in Electro-Optics

by

Leonel Pastor Gonzalez


UNIVERSITY OF DAYTON

Dayton, Ohio


May 2009

ACCURATE DETERMINATION OF NONLINEAR OPTICAL PARAMETERS
OF SEMICONDUCTORS AT INFRARED WAVELENGTHS


APPROVED BY:




Peter E. Powers, Ph.D.
Advisor Committee Chairman
Professor, Physics



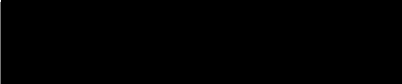
Joseph W. Haus, Ph.D.
Committee Member
Professor and Director, Electro-Optics



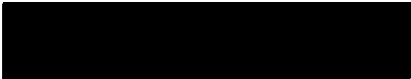
Shekhar Guha, Ph.D.
Committee Member
Research Scientist, Air Force Research
Lab




Andrew Sarangan, Ph.D.
Committee Member
Associate Professor, Electro-Optics



Paul T. Murray, Ph.D.
Committee Member
Professor, Dept. of Graduate Materials
Engineering



Malcolm W. Daniels, Ph.D.
Associate Dean
School of Engineering



Joseph E. Saliba, Ph.D., P.E.
Dean
School of Engineering

ABSTRACT

ACCURATE DETERMINATION OF NONLINEAR OPTICAL PARAMETERS OF SEMICONDUCTORS AT INFRARED WAVELENGTHS

Name: Gonzalez, Leonel Pastor
University of Dayton

Advisor: Dr. Peter E. Powers

Nonlinear optics covers the vast field of irradiance dependent interactions between light and materials, including generation of light in a second order medium through processes such as optical parametric oscillation or self attenuation of light in a third order medium. It is important to determine the relevant material parameters which control the efficiency of the interactions. In extracting material parameters from experimental results, many assumptions of questionable validity are often made to simplify calculations. In this work, a numerical model was developed, with as few assumptions on laser beam parameters as possible, to describe the interactions of arbitrary, complex four dimensional electro-magnetic fields with a nonlinear medium.

Second harmonic generation (SHG) is a second order nonlinear optical phenomenon in which an incident light beam at one frequency generates light at twice the frequency. In this work, SHG in a newly grown material, CdSiP₂ was investigated and the first efficient harmonic generation in this crystal was accomplished at a mid-wave infrared wavelength. Excellent agreement between experimental results and theory was obtained, with no free parameters, using a numerical model which accurately modeled spatial and temporal beam profiles.

An area of third order nonlinear optics is self action, where nonlinear absorption and refraction in a medium are dependent on the irradiance of the incident light. Nonlinear absorption in semiconductors is a coupled process where intrinsic two photon absorption generates free carriers which in turn modify the linear absorption via free carrier absorption. In addition, the generated free carriers alter the phase of the beam through nonlinear refraction. Thermal effects also play a role since the nonlinear absorption leads to heat rise within the material which in turn generates a thermal lens. All of these coupled processes occur simultaneously in the nonlinear medium. Investigation of these effects in the semiconductor InP was conducted and for the first time, a self consistent set of intrinsic two photon absorption coefficients and free carrier nonlinear absorption cross-sections were found at two different infrared wavelengths. Values of the free carrier absorption coefficients of InP determined by nonlinear absorption measurements have not been previously reported.

To my wife, Trina, and children, Noah, Ian & Connor. This is for them.

ACKNOWLEDGMENTS

This dissertation would not be possible without the assistance of numerous people. First and foremost I would like to thank Shekhar Guha, with whom I have had the pleasure of working with for over seven years now. I am deeply grateful for the opportunities I have had to learn and grow and the freedom to pursue this endeavor.

To Prof. Peter Powers, my University of Dayton advisor during my return to graduate school. Thank you for formally teaching me nonlinear optics, I've been able to make a career out of it.

I would like to thank the Air Force Research Lab, General Dynamics Corporation (formerly Anteon), and the Dayton Area Graduate Studies Program (DAGSI) for financial support throughout this research. Without these groups this work would not have been possible.

Thanks to the IR Lab team: Jacob, Derek, Jean, Amelia, Joel and Emily for all of their support and assistance.

Thanks to Robert Hull and Mike Lander of General Dynamics for giving me the opportunity to return to Dayton and the freedom to do my job. To Daniel Seibert, also of General Dynamics, for his electronic wizardry. A true jack of all trades.

I have had the pleasure to have learned from, and continue to interact with, Prof. Qin (Tim) Sheng, formerly of the University of Dayton and currently at Baylor University. I appreciate and have put to good use the numerical methods he has taught me.

I appreciate all the insightful conversations I've had, and continue to have, with Srinu Krishnamurthy and Zhi-Gang Yu of SRI. I appreciate the semiconductor insight I have learned and always look forward to our meetings.

To my parents, Julia and Eduardo Gonzalez, who came to this country with very little, gave me so much and have always supported and encouraged me in all of my endeavors, *Gracias para todo*

To my children, Noah, Ian and Connor, who have truly shown me what the most important things in life are, I hope all of you grow up chasing your dreams.

And most especially my love, my life, my wife, Trina, thank you for everything

TABLE OF CONTENTS

	Page
Abstract	iii
Dedication	v
Acknowledgments	vi
List of Figures	xi
List of Tables	xiv
CHAPTERS:	
I. INTRODUCTION	1
1.1 Aims of this Work	1
1.2 Dissertation Outline and Relevant Publications and Presentations	2
1.3 Additional Work Outside the Scope of this Dissertation	3
II. BACKGROUND AND MOTIVATION	5
2.1 Introduction	5
2.2 Overview of Research Related to Nonlinear Absorption and Refraction	9
2.3 Review of Nonlinear Absorption Values for InP	12
2.4 Measurement Techniques for Characterization of Nonlinear Absorption and Re- fraction	15
III. THEORY	20
3.1 Introduction	20
3.2 Wave Equation with Nonlinear Source Term	20
3.3 Wave Equation for Second Order Nonlinearities: Second Harmonic Generation with Walkoff	23
3.3.1 Ordinary Polarized Beam	24
3.3.2 Extraordinary Polarized Beam with Walkoff	25
3.4 Third Order Optical Nonlinearities in Semiconductors	27

3.4.1	Wave Equation with Bound Electronic, Free Carrier and Thermal Non-linearities	27
3.4.2	Charge Carrier Generation	30
3.4.3	Heat Equation	30
IV.	NUMERICAL METHOD	31
4.1	Introduction	31
4.2	$\chi^{(2)}$ Second Harmonic Generation	32
4.2.1	Solution of the \hat{P} Operator	34
4.2.2	Solution of the \widehat{NL} Operator	36
4.3	$\chi^{(3)}$ Nonlinear Absorption and Refraction	37
4.3.1	Solution of the \hat{P} operator	40
4.3.2	Solution of the \widehat{NL} operator	41
4.4	Phase Retrieval	42
V.	APPLICATION OF BEAM PROPAGATION MODELING TO SECOND HARMONIC GENERATION IN CdSiP ₂	47
5.1	Introduction	47
5.2	Optical Properties	47
5.3	Experimental Layout	50
5.4	SHG Theory and Numerical Model	51
5.5	Experimental and Theoretical Results	52
5.5.1	SHG Theoretical Optimization	55
5.6	Conclusion	57
VI.	INTRINSIC TWO PHOTON AND FREE CARRIER NONLINEARITIES IN InP	58
6.1	Introduction	58
6.2	Theory and Numerical Modeling	60
6.3	Linear Transmission and Free Carrier Absorption	62
6.4	Nonlinear Absorption in InP	64
6.4.1	Experiment and Analysis	64
6.4.2	Results at 77 K	70
6.5	Nonlinear Refraction in InP	71
6.5.1	Theory and Numerical Modeling	71
6.5.2	Experimental Results and Analysis	72
6.6	Conclusion	74
VII.	CONCLUSION	76

7.1 Summary	76
7.2 Future Work	77
Bibliography	78

LIST OF FIGURES

<u>Figure</u>	<u>Page</u>
2.1 Transmission and absorption spectra of bulk InP	6
2.2 Schematic of possible optical interactions within a semiconductor	8
2.3 Nonlinear transmission due to two photon absorption	9
2.4 Theoretical wavelength dispersion of β for a variety of different bandgap semiconductors	11
2.5 Theoretical wavelength dispersion of β in InP based on parabolic and full band modeling	14
2.6 Theoretical dispersion of the free carrier absorption for holes in InP based on full band modeling	15
2.7 Dispersion of β for CdTe and CdMgTe	16
2.8 Comparison of theoretical Z and I -scan results for the same maximum peak irradiance at focus	17
2.9 I -scan results using aberrated beams	19
3.1 Schematic of walk-off direction within crystal and lab reference frame	26
4.1 Beam images used for phase retrieval at $Z = 10$ and 14 cm. Bottom image is the numerically retrieved phase at $Z = 10$ cm.	45
4.2 Beam images at $Z = 54$ cm. Actual beam image (left) and numerical result (right) are shown.	45

4.3	Horizontal slice through the centers of the actual camera image at $z = 54$ cm (red) and the numerical result at $z = 54$ cm after propagation of the amplitude and phase information found at $z = 10$ cm	46
5.1	CdSiP ₂ Type I phasematching curve at a pump wavelength of $2.39 \mu\text{m}$	48
5.2	Image of CdSiP ₂ crystal 11B used for second harmonic generation experiments . .	49
5.3	Measured absorption spectra for o and e polarized light for CdSiP ₂ sample 9A. . .	49
5.4	Experimental SHG/FHG layout. A TEA CO ₂ laser pumps two AgGaSe ₂ crystals to generate $4.78 \mu\text{m}$ light. This is then used as the pump source for second harmonic generation experiments in the CdSiP ₂ crystal.	50
5.5	Orientation of o and e polarized light in CdSiP ₂ and dependence of conversion efficiency on angle of incidence	53
5.6	Second harmonic output energy external conversion efficiency at $2.39 \mu\text{m}$ as a function of incident pump energy from a CdSiP ₂ crystal.	54
5.7	Temporal profile of the input $4.78 \mu\text{m}$ pump beam and the theoretical output of the generated signal and depleted pump beams.	55
5.8	SHG conversion efficiency in uncoated CdSiP ₂ as a function of incident pump beam spot size. Solid lines end at the same fluence/irradiance value.	56
5.9	SHG output energy in CdSiP ₂ as a function of incident pump beam ellipticity. Pump beam radii were chosen such that peak irradiance remained constant at 3 mJ of pump energy. Crystal walk-off is in the x-axis plane.	57
6.1	Nonlinear absorption in InP at $1.064 \mu\text{m}$ for different pulse durations. As the pulsewidth increases, contributions from free carrier absorption becomes significant.	62
6.2	Transmission spectra of undoped and Fe doped InP samples used for NLA measurements. Undoped samples have multi-layer AR coatings while the Fe sample has a single layer coating.	63
6.3	Transmission spectra of Zn doped InP samples and average hole free carrier absorption cross section.	64

6.4	Nonlinear absorption results (open symbols) at 1.064 μm on undoped InP samples. Solid lines are theoretical results using values of $\beta = 25.5 \text{ cm/GW}$ and $\sigma_{\text{abs}} = 1.5 \times 10^{-17} \text{ cm}^2$ for all data.	67
6.5	Nonlinear absorption results (open symbols) at 1.535 μm on undoped InP samples. Solid lines are theoretical results using values of $\beta = 14.6 \text{ cm/GW}$ and $\sigma_{\text{abs}} = 7.2 \times 10^{-17} \text{ cm}^2$ for all data.	68
6.6	Output traces for undoped (left) and Fe doped (right) InP samples at similar incident irradiances. Input wavelength is 1.535 μm , $t_0 = 50 \text{ ns}$	69
6.7	Nonlinear absorption in undoped (triangles) and Fe (circles) doped InP at 1.535 μm , $t_0 = 50 \text{ ns}$. Values of β and σ_{abs} used for both samples are the same. Lifetime in Fe:InP is set to 3 ns and greater than t_0 for the undoped sample.	69
6.8	Nonlinear absorption in 0.96 mm, undoped InP at room temperature (red) and 79 K (blue). Data was taken at 1.064 (left) and 1.535 (right) μm using the ns lasers. Values of β and σ_{abs} at 79 K are indeterminate.	70
6.9	Beam image from camera (left) and modeling results (center) at plane Z_2 for an incident irradiance of 79 MW/cm^2 . Graph (right) shows a comparison of the horizontal line profiles through the center of both images.	73
6.10	Array of beam images from camera (left) and modeling results (center) at plane Z_2 for incident irradiances of 3 (bottom) to 43 MW/cm^2 (top). Graphs (right) show a comparison of the horizontal line profiles through the center of both images.	75

LIST OF TABLES

<u>Table</u>	<u>Page</u>
1.1 Dissertation related publications and presentations	3
2.1 Experimentally published values of β for InP	13
5.1 CdSiP ₂ material parameter values used in modeling of SHG interaction	54
6.1 Comparison of σ_h [$\times 10^{-17} \text{cm}^2$] values at 1.064 and 1.535 μm from linear transmission measurements	64
6.2 Values of β and σ_{abs} at 1.064 and 1.535 μm	66

CHAPTER I

INTRODUCTION

1.1 Aims of this Work

The aim of this work was to develop a method to accurately measure nonlinear optical parameters of materials for nonlinear effects that are initiated through a two-photon absorption process, and for pulses of nanosecond or longer duration, free carrier nonlinearities may become dominant. This was achieved through theoretical modeling of 3rd order instantaneous and induced optical nonlinearities in semiconductors and the effects on an electro-magnetic beam as it propagates within and beyond the sample, and also through detailed experiments. Both the spatial and temporal properties of the laser beam used for the measurements were accurately measured and modeled.

A four dimensional (x, y, z, t) numerical model which can handle arbitrary spatial profiles of the field amplitude and phase, as well as actual temporal profiles was developed. A method to recover both the amplitude and phase of the incident field has also been implemented. The method developed for characterizing 3rd order nonlinearities was applied to analyze the results of second harmonic generation experiments performed with a newly grown crystal. For this application, the code was modified to include the effects of beam walk-off and pump depletion. Experimental results and theoretical modeling were in excellent agreement using all known parameters (i.e. with no free

parameters in the model). Throughout this work, in modeling both 2^{nd} and 3^{rd} order optical nonlinearities, every effort has been made to minimize experimental assumptions and approximations of the incident and transmitted beams.

1.2 Dissertation Outline and Relevant Publications and Presentations

The overall outline of the dissertation is as follows. Chapter 2 describes 3^{rd} order nonlinear optical processes within a semiconductor and focuses on two photon absorption. A review of relevant research in the field is discussed. A discussion on the commonly used Z -scan technique is provided which then leads to a description of the irradiance, or I -scan, method which was developed. Advantages and limitations of both methods are discussed.

Chapter 3 derives the 2^{nd} and 3^{rd} order nonlinear wave equations used. Only the slowly varying envelope approximations are made. The wave equation specific to second harmonic generation in a Type I crystal with walk-off is included. The 3^{rd} order wave equation is for irradiance dependent nonlinear absorption and refraction at a single wavelength. Coupled, nonsteady state equations for generated free carriers and heat rise are presented.

Numerical methods of solving the nonlinear partial differential equations from Ch. 3 are presented in Ch. 4. Chapter 4 also includes a derivation of the split step method used, allowing diffraction and nonlinearities to be numerically modeled independently. In addition, forward difference methods are used to solve the free carrier and thermal rate equations in third order processes is described. A forward difference method to numerically solve the nonlinear coupling in second harmonic generation is also described. The last part of Ch. 4 discusses the phase retrieval method used.

Table 1.1: Dissertation related publications and presentations

Chapter	Presentations and/or Publications
1 Introduction	
2 Background and Motivation	2004 CLEO presentation, ^a OSA proceedings [1] ^a Appl. Phy. Lett. [2] ^b , J. Appl. Phy. [3] ^b SPIE proceedings [4] ^a
3 Wave Equations	
4 Numerical Method	2007 ICIAM presentation ^a PAMM proceedings ^a [5]
5 SHG in CdSiP ₂	2009 Phot. West presentation ^a SPIE proceedings [6] ^a
6 NLA & NLR InP	2009 NLO conf. [7] ^c Optics Express [8] ^c
7 Conclusion	

^a presenter and/or author^b co-author ^c submitted

Chapter 5 presents experimental and modeling results of second harmonic generation measurements on a CdSiP₂ crystal. Methods of enhancing the conversion efficiency are investigated. Chapter 6 is a thorough discussion of the measurement and analysis of nonlinear absorption and refraction in InP. Measurements were done at two wavelengths and at both room and cryogenic temperatures in order to determine both the wavelength and temperature dependencies of the nonlinearities.

Table 1.1 lists an overview of the main chapter topics with relevant publications and presentations.

1.3 Additional Work Outside the Scope of this Dissertation

During the period of course-work and research for this dissertation, parallel experiments were conducted resulting in additional presentations and publications. Since these works were indirectly associated with this dissertation, they will be briefly mentioned here but not discussed further. Much

of the research in this parallel work has aided in the understanding and modeling of the nonlinear effects discussed in this dissertation.

In the following works the candidate was a co-author: Investigations of bulk InGaSb have been published in [9] and [10]. Measurement of the damage thresholds in ceramic Nd:YAG laser host material were published in conference proceedings [11, 12]. Optical properties of vanadium oxide films was published in [13]. Thermo-optical material characterization was published in [14]. Paraxial light propagation studies were reported in [15], [16] and [17]. The candidate was a presenter and author on a conference paper investigating nonlinear effects in GaP, [18]. In addition, candidate was presenter, author and/or co-author on over five papers given at various Military Sensing Symposia (MSS) over the years 2004 through 2009. In addition, reviewed a paper for the journal Applied Physics Letters, which was published in early 2008. Lastly, the candidate helped supervise and was a committee member for, a recent M.S. Electro-Optics graduate [19].

CHAPTER II

BACKGROUND AND MOTIVATION

2.1 Introduction

Light having a wavelength λ (i.e., a photon having energy $E_p = hc/\lambda$) falling on a semiconductor crystal with a bandgap E_g is strongly absorbed if $E_p > E_g$, i.e., $\lambda < \lambda_g$, where $\lambda_g = E_g/hc$. This is shown in Fig. 2.1 by the transmission spectrum of a single crystal sample of the semiconductor InP, with $E_g = 1.344$ eV at room temperature ($\lambda_g = 0.922 \mu\text{m}$). Below $0.922 \mu\text{m}$, the sample transmission is low due to linear, one photon absorption, and above $0.922 \mu\text{m}$, i.e., for $E_p < E_g$, the transmission value is high, about 60% for a sample polished on both sides. The 40% loss in transmission is due to reflection from the two surfaces.

The above situation is valid for light from ordinary sources, such as ambient light or from lamps in a spectrometer, for irradiance levels below tens of kilowatts per cm^2 . For high irradiance laser light, typically above 100's of kilowatts to megawatts per cm^2 , the absorption by the semiconductor can become high, even for $E_p < E_g$, i.e., $\lambda > \lambda_g$. This is due to nonlinear optical processes such as multi-photon absorption (MPA) and associated absorption processes initiated by MPA. Of all the nonlinear optical processes, two photon absorption (TPA) can be observed at the lowest levels of irradiance, provided the photon energy is greater than half the bandgap energy, i.e., $E_p > E_g/2$. Thus TPA is the dominant nonlinear optical process for wavelengths $\lambda < 2\lambda_g$. For photon energies

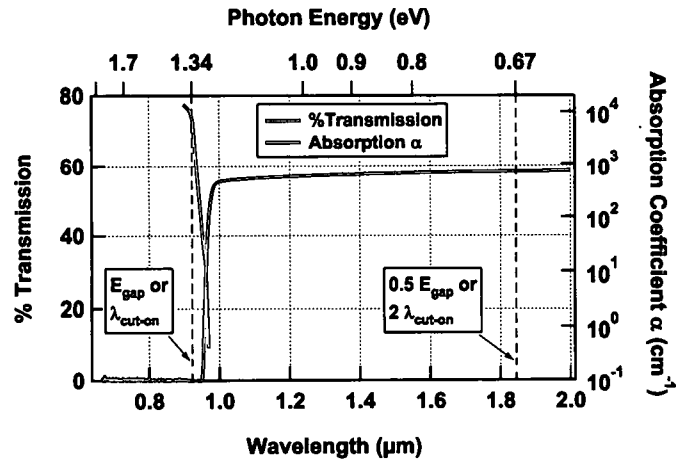


Figure 2.1: Transmission spectra (blue) of a 1mm thick, uncoated InP sample. Near band gap absorption is given by the red trace.

between $E_g/3$ and $E_g/2$, the dominant nonlinear absorption arises from three photon absorption (3PA).

For laser pulses of nanosecond or longer duration, although multiphoton absorption processes (2PA, 3PA, etc.) initiate the nonlinear optical absorption in semiconductors, as the irradiance of light increases, the absorption effects arising from free carriers (electrons or holes) created by the MPA process become dominant. The free carrier absorption coefficient, denoted by σ_{abs} (or σ_{FCA}) is an important nonlinear absorption parameter of a semiconductor.

In addition to nonlinear absorption, nonlinear refraction, i.e. an irradiance dependent change of refractive index, plays an important role in interaction of semiconductors with high irradiance laser beams. A parameter γ characterizes the irradiance dependent refractive index change arising from distortion of bound electron orbits. The free carriers generated by NLA also cause irradiance

dependent refraction. This is characterized by the parameter σ_{ref} (or dn/dN , the differential amount of refractive index change per unit change in generated carrier concentration).

In addition to β and γ , free carrier and thermal effects can also contribute to the overall nonlinearities. For pulse widths on the order of a few ps and longer, free carrier contributions become significant for both NLA and NLR. Heat rise due to linear and nonlinear absorption also effects the NLR, but these contributions become significant for pulses of ns durations and longer.

Figure 2.2 shows a diagram of possible optical interactions due to high irradiance light, as from a laser, within a semiconductor. It has been modified with permission from the author [20]. As shown in the diagram, multiple interrelated physical processes take place within the semiconductor. For a laser which has propagated through a semiconductor, it is difficult to determine what factors contributed to the observed NLA and NLR of the exit beam by direct measurement. Being able to model the effects and construct the appropriate experiments to identify and differentiate them is an ongoing task in the literature and one of the aims of this research.

The equation describing propagation of an electromagnetic field through a semiconductor is given as

$$\frac{\partial A}{\partial z} = \frac{i}{2k_0} \nabla_{\perp}^2 A + \frac{2i\pi}{\lambda} (\Delta n + \gamma I) A - (\alpha_0 + \Delta\alpha + \beta I) \frac{A}{2} \quad (2.1)$$

which is derived in the next chapter. This equation is coupled to the generated free carriers, N , and heat rise, ΔT through

$$\frac{dN}{dt} = \frac{\alpha I}{h\nu} + \frac{\beta I^2}{2h\nu} - \frac{N}{\tau} \quad (2.2)$$

$$\frac{\partial \Delta T}{\partial t} = \frac{1}{\rho c} ((\alpha + \sigma_{\text{abs}} N) I + \beta I^2) \quad (2.3)$$

Equations (2.1) through (2.3) form a set of coupled nonlinear partial differential equations. Solution of these coupled equations is done via numerical methods discussed in Ch. 4. A more common form

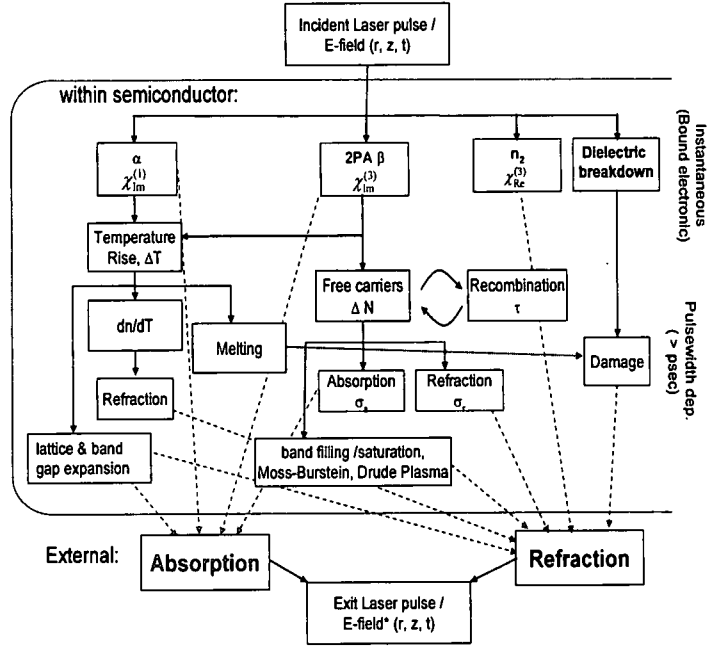


Figure 2.2: Schematic showing linear and nonlinear optical interactions possible within a semiconductor. Both instantaneous, bound electronic effects, as well as slower contributions from thermal and free carrier nonlinearities may be present.

of (2.1) relating the field in terms of irradiance is

$$\frac{dI}{dz} = -(\alpha + \sigma_{\text{abs}}N)I - \beta I^2 \quad (2.4)$$

If the pulse width is sufficiently short such that no free charge carriers are generated ($N = 0$), and assuming the irradiance is

$$I(r, t) = I_0 e^{-\left(\frac{r}{r_0}\right)^2} e^{-\left(\frac{t}{t_0}\right)^2} \quad (2.5)$$

an analytical solution for the transmission based on Equation (2.4) can be derived [21]

$$T = \frac{1}{\sqrt{\pi}Q} \int_{-\infty}^{\infty} \ln \left[1 + Q e^{-\left(\frac{t}{t_0}\right)^2} \right] dt \quad (2.6)$$

where Q is a dimensionless parameter ($Q = \beta I_0 L$), and where L is the sample length. This assumes a sample with no surface or absorptive losses. Figure 2.3 shows a plot of transmission from (2.6) as a function of Q . In any 2PA measurement, results which fall below the curve indicate the presence of free carrier absorption.

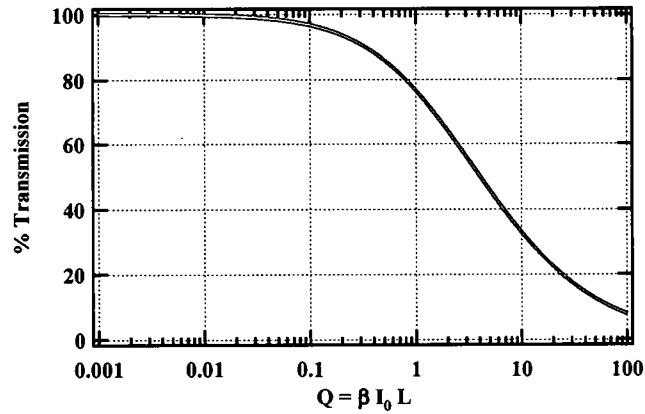


Figure 2.3: Nonlinear transmission due to two photon absorption. Parameter $Q = \beta I_0 L$

2.2 Overview of Research Related to Nonlinear Absorption and Refraction

Soon after the discovery of the first laser, nonlinear effects such as harmonic generation and irradiance dependent absorption were postulated by Braunstein [22] in 1962. Two years later the first observation of irradiance dependent, 2PA in a semiconductor was observed by Braunstein and Ockman [23]. Since that time, much research has been done in the area of semiconductor optical nonlinearities. [22]

As technology advanced, shorter laser pulse widths, and higher pulse irradiances, became more readily available to researchers. In 1985, VanStryland and co-workers [24] presented results of nonlinear absorption and refraction measurements on a variety of semiconductors. Bandgap energies of the semiconductors varied from 1.4 to 3.7 eV (885 to 335 nm). Using the fundamental and second harmonic wavelengths of a picosecond pulse duration Nd:YAG laser, VanStryland et al. compared the 2PA coefficients of ten semiconductors. Based on a parabolic model of the conduction and valence bands, they found that the nonlinear absorption coefficient, β , was proportional to E_{gap}^{-3} . They gave the wavelength dependence of β as:

$$\beta(\omega) = K \frac{\sqrt{E_p}}{n^2(\omega)E_{\text{gap}}^3} F_2 \left(\frac{\hbar\omega}{E_{\text{gap}}} \right) \quad (2.7)$$

where K is a material independent collection of constants. The authors used a best fit value of $K = 3100$. The Kane energy, E_p , is approximately material independent and set to 20.7 eV, E_{gap} is the bandgap energy in eV and n is the refractive index of the semiconductor. The parameter F_2 , which is a function of the frequency of the incident light and the bandgap of the material, is dependent on the band structure model used. Assuming a parabolic band structure, the F_2 function is:

$$F_2(x) = \frac{(2x - 1)^{\frac{3}{2}}}{(2x)^5} \quad (2.8)$$

Using the values of K and E_p given previously, Equation (2.7) returns a value for β in units of [cm/GW] as a function of wavelength. Figure 2.4 shows the theoretical wavelength dispersion of β for a variety of different bandgap materials. As the material E_{gap} decreases, a large increase in the value of the 2PA coefficient is expected.

In 1989, Sheik-Bahae and coworkers [25] published a paper on a novel method to measure the nonlinear refractive index (γ). Their method, known as the Z -scan, is a common technique used

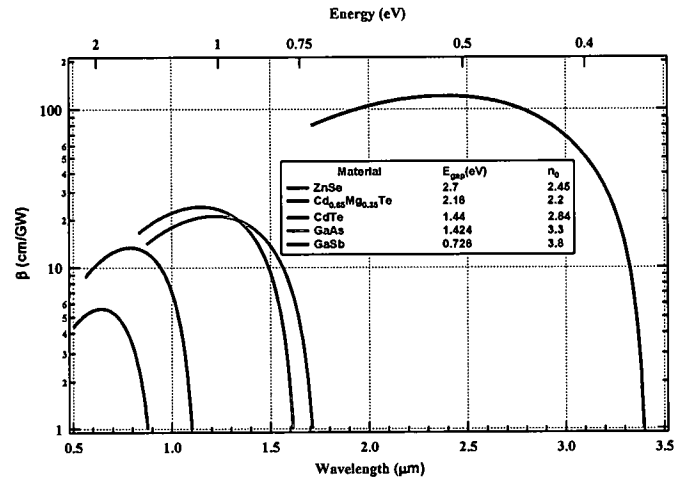


Figure 2.4: Theoretical wavelength dispersion of β for a variety of different bandgap semiconductors.

today. There are many variations on the technique but all are based on translating a sample through the focus of a laser beam and observing the change in the far-field irradiance. In 1990 Sheik-Bahae and coauthors modified their *Z*-scan method to include nonlinear absorption as well [26]. The following year, theoretical work on the wavelength dispersion of γ was published [27].

From the early work of Miller on InSb, through VanStryland and Sheik-Bahae's work in the late 1980's and early 90's, and still ongoing for many of these authors today, investigation of NLA and NLR in semiconductors is a vast field. As the years progress and experiments become more refined, the values of the nonlinear coefficients are continuously corrected. The semiconductor InAs provides an example of this. In addition to Murdin's work in 1993, Berryman and Rella also did a thorough study of the nonlinear absorption of InAs using a free-electron laser [28]. They probed the material and investigated its NLA behavior at three wavelengths as well as its temperature dependence. Instead of assuming a parabolic band, they were able to discriminate between parabolic

and non-parabolic band effects. In addition they measured free-carrier absorption and reported on evidence of higher order absorption processes. An investigation on nonlinear refraction near the absorption edge in InAs was carried out by Poole and Garmire in 1984 [29].

There are even more recent investigations of InAs, one of which is a PhD dissertation by Corbett [20]. While most of the prior work on InAs was done using picosecond and longer lasers, the influence of free carriers was sometimes ignored, or assumed to be minimal. While this may hold somewhat for short picosecond lasers, the effect can not be ignored at longer pulse durations. Corbett used a fs laser with a tunable difference frequency generation stage to investigate dispersion of β and γ . Such short pulses prevented free-carrier effects from effecting the observed nonlinearities.

In 2006, Haeri and co-authors [30] used a frequency doubled CO₂ with a pulse width of 200 ns, they studied NLA and NLR in InAs while including free carrier contributions. Krishnamurthy and co-authors [2] also investigated NLA in InAs. Nonlinear absorption coefficients as well as free carrier and Auger and radiative recombination lifetimes were calculated as functions of wavelength, temperature and carrier density based on a full band structure model. Experimental observations of the temporal change in transmission were modeled based on this theory.

2.3 Review of Nonlinear Absorption Values for InP

Theoretical and experimental results to determine β in InP have been reported, although none of these report a value for the free carrier absorption (FCA) cross section, σ_{abs} , although FCA effects are acknowledged in [31]. Table 2.1 lists experimentally measured values of β reported in the literature. Results of Vignaud [34] and Tiedje [33] are based on pump-probe measurements using fs duration pump sources. Dvorak [32] used a 100 ps laser source in a closed aperture Z -scan measurement. These results all use indirect methods to measure the nonlinear transmission.

Table 2.1: Experimentally published values of β for InP

$\lambda(\mu\text{m})$	$\beta (\frac{\text{cm}}{\text{GW}})$
1.064	90 [32]
	210 [31]
1.3	70 ± 18 [33]
1.55	24 - 33 [34]

The work of Lee and Fan [31] was a direct measurement of the transmission, but used laser pulse durations on the order of 30 ns. For pulse durations of 100 ps and longer, as will be shown in Ch. 6, FCA plays a dominant role in the NLA, yet these effects were not properly accounted for.

In addition to experimental results, a large variation in the theoretical values have also been reported. A review paper by Vaidyanathan et.al. [35] reports theoretical 2PA values on a variety of semiconductors based on different theoretical approaches. For InP, using different assumptions in the theoretical models, they predict β values at $1.064 \mu\text{m}$ in the range of 26 to over 300 cm/GW. Theoretical values of β at other wavelengths are not available in the literature. Recent work by Krishnamurthy, based on the methods in [3] and recently applied to InP [36] predicts lower values of β than have been previously reported. Values on the order of 25 and 13 cm/GW at 1.064 and $1.55 \mu\text{m}$ are predicted. It should be noted that the work of Krishnamurthy is closely associated with much of the investigation in this dissertation. Figure 2.5 is a graph of the theoretical values of β from [36] as well as from the parabolic band model from Eq. 2.7.

For pulsewidths of significant pulse duration, as photons are absorbed via 1PA (if present) or 2PA, the photo generated electrons and holes are excited into the conduction and valence bands respectively. Once there, these free carriers are free to absorb via a 1PA process (an excited state absorption). The total excited state absorption is characterized by the free carrier cross sections of

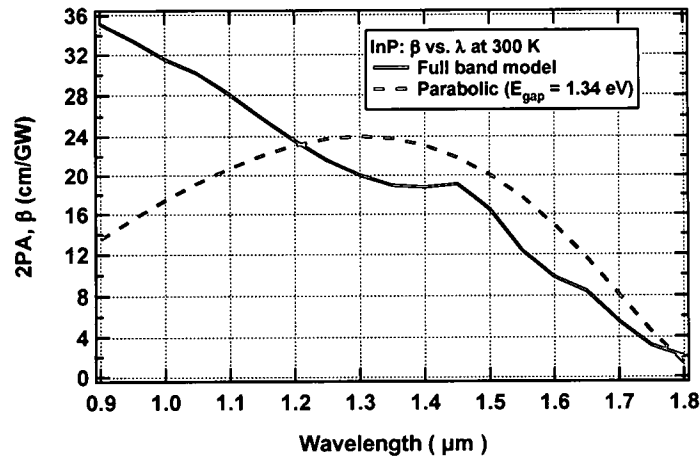


Figure 2.5: wavelength dispersion of β in InP. The dashed line is based on the parabolic band assumption while the solid line is based on a full band structure model.

both electrons and holes ,

$$\sigma_{\text{tot}} = \sigma_h + \sigma_e \quad (2.9)$$

times the number of generated carriers, $\Delta N_{e,h}$. Since equal numbers of holes and electrons are generated, $\Delta N_e = \Delta N_h = \Delta N$. Although equal numbers of electrons and holes are created, FCA is predominately due to hole absorption since $\sigma_h \gg \sigma_e$. The free carrier cross section is wavelength dependent and follows a power law with wavelength. A theoretical dispersion curve of σ_h from [36] is shown in Fig. 2.3. Note that in free carrier absorption takes place at all wavelengths, and not just the wavelengths restricted to the multiphoton absorption bands (i.e. between λ_{gap} and $2\lambda_{\text{gap}}$ for two photon absorption, λ_{gap} and $3\lambda_{\text{gap}}$ for 3PA etc.). One of the goals of the work in Ch. 6 is to independently measure the values of the β and σ_{tot} coefficients and to compare them with the theoretical values. A technique that has been developed to accurately measure NLA and NLR, known as the I , or irradiance scan, method, is the topic of the last section in this chapter.

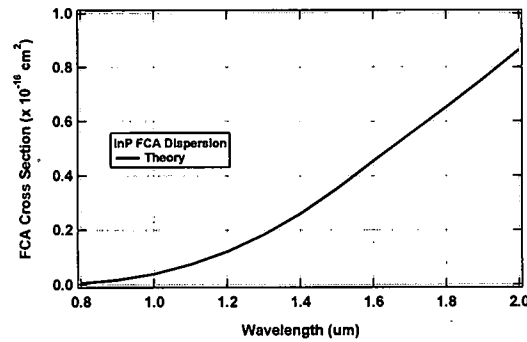


Figure 2.6: Theoretical dispersion of the free carrier absorption for holes in InP based on full band modeling in the regime of 2PA.

2.4 Measurement Techniques for Characterization of Nonlinear Absorption and Refraction

The Z -scan is a popular method [25] used for measurement of 3rd order optical nonlinearities of a material and involves translating a ‘thin’ slab of the material through the focus of a laser beam and measuring the total energy transmission as well as the energy transmitted through an aperture. The sample is usually translated multiple confocal distances on either side of focus, forcing the detectors to be placed in the far field. One of the assumptions in the analysis of Z -scan data is that the irradiance and phase of the incident beam are Gaussian in nature

For measurements of the nonlinearities at cryogenic temperatures, this method is difficult to implement since it usually involves translation of a liquid nitrogen filled dewar, along with its vacuum attachments, through the focal region. The body of the dewar, typically inches in length between the entrance and exit windows, may limit the distance over which the sample can be translated. Moreover, if the sample or dewar windows are wedged, even by a small angle, translating them can

cause deflection of the laser beam away from the closed aperture detector causing variation of the signal with sample position, which could be misinterpreted as coming from sample nonlinearities.

A similar but alternate technique for the measurement of optical nonlinearities in which neither the sample nor the detector is moved is presented here. It is similar to the I-scan first presented by Taheri [37], however for this work, the sample is placed at the beam waist and the total energy transmission through the sample is measured as a function of the incident irradiance, along with the value of the on-axis fluence measured at a distance ideally less than the Rayleigh range of the beam.

Nonlinear absorption measurements on CdTe and CdMgTe using the *I*-scan technique are shown in Fig.2.7. This work, which was conducted during the early stages of the dissertation, used a tunable ps laser source and assumed no FCA. The β values were determined by numerical fitting of Eq. (2.6). Later analysis into the temporal dependence of NLA between 2PA and FCA led to the realization that FCA should be accounted for at pulse durations of 10 ps and longer.

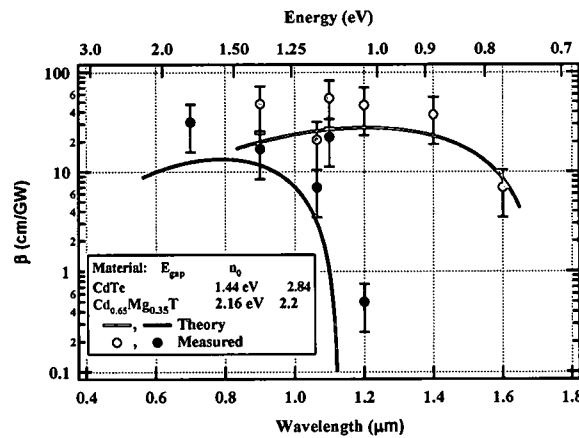


Figure 2.7: Experimentally measured values of β at wavelengths across the 2PA region for CdTe and CdMgTe samples.

This realization led to development of an early numerical code which modeled Equations (2.4) and (2.2). This code allowed analysis of both open aperture energy transmission, NLA, as well as on-axis fluence, NLR. It was found that one of the advantages of the I scan method was the ability to measure a larger variation in the NLR signal since the on-axis detector could be placed in the near field, instead of multiple Rayleigh ranges away. Theoretical results showing NLA and NLR effects for both a Z and I scan are shown in Fig. 2.8. In both cases, the peak irradiance at focus is the same. In the case of the Z scan, the sample is translated ± 4.5 Rayleigh ranges with the detectors placed at ± 5 Rayleigh ranges. However, by placing the detectors at one Rayleigh range, a larger change in the NLR signal could be observed for the same irradiance. For the I scan, the sample is fixed at focus and the incident irradiance is varied up to the peak irradiance with the closed aperture detector placed at half a Rayleigh range behind the sample or dewar.

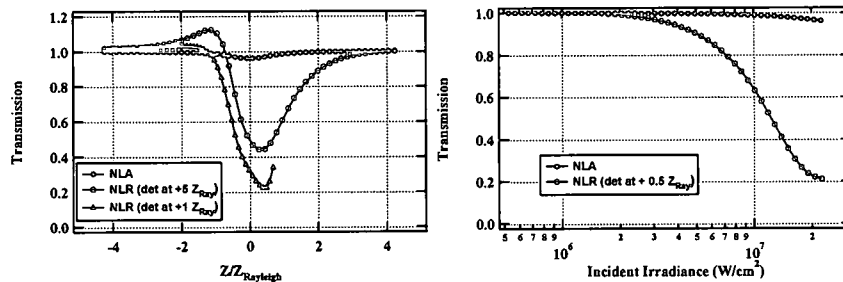


Figure 2.8: Comparison of theoretical Z and I -scan results for the same maximum peak irradiance at focus. Z results are for the closed aperture detector placed at 5 and 1 times the Rayleigh range. I -scan results are with the closed aperture detector placed at half a Rayleigh range.

With a method available to analyze the experimental data, data was collected on a variety of semiconductors using a ps $1.064\ \mu\text{m}$ laser at room and cryogenic temperatures. Some of this experimental data and analysis has been published in [4], and also lead to the successful completion of an M.S. degree in Electro-Optics by a recent student [19].

Although this method was useful, difficulty arose when measuring NLR with beams which were not perfectly diffraction limited. This was evident in analysis of data where the laser source was the $1.57\ \mu\text{m}$ signal output of a ns optical parametric oscillator. While good agreement to the NLA data could be obtained, it was difficult to determine values of the NLR coefficients which accurately described the data. The experiment was repeated by removing the on-axis fluence detector and replacing it with a two dimensional pyro-electric array (Spiricon Pyrocam III) which allowed the beam profile to be measured at the location of the closed aperture detector. These results are shown in Fig. 2.9.

After this realization, it was concluded that accurate analysis of the NLR data required numerical modeling of the two dimensional beam profile and knowledge of both the amplitude and phase since determination of the NLR coefficient requires propagation of the beam beyond the sample. This led to development of the four dimensional numerical code and implementation of a phase retrieval routine which are described in Ch. 4. For the NLR analysis in Ch. 6, closed aperture measurements were not conducted, instead the propagated beam profiles were recorded and the numerical model was used to predict these profiles by best fit of the NLR coefficients.

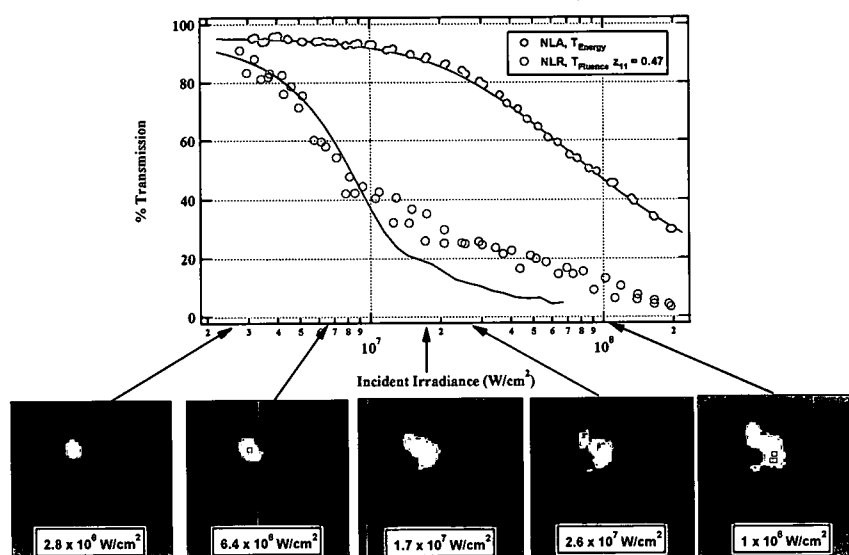


Figure 2.9: Typical *I*-scan results when using aberrated beams. Beam images and NLR data were taken in the near field at distance of half a Rayleigh range

CHAPTER III

THEORY

3.1 Introduction

This chapter focuses on derivation of the nonlinear wave equations used within this dissertation. The second order, $\chi^{(2)}$, process investigated will be second harmonic generation (SHG) with walk-off. Third order, $\chi^{(3)}$, wave equation derivation will focus on self action of a single field which experiences nonlinear absorption (NLA) and nonlinear refraction (NLR). Coupled rate equations for carrier generation and heat rise will also be given. The $\chi^{(2)}$ and $\chi^{(3)}$ wave equations derived here form the basis of the numerical modeling discussed in Ch. 4 and analysis of the experimental results in Chapters 5 and 6.

3.2 Wave Equation with Nonlinear Source Term

Beginning with Maxwell's equations

$$\nabla \times \mathbf{H} = \frac{\partial \mathbf{D}}{\partial t} \quad (3.1)$$

$$\nabla \times \mathbf{E} = -\frac{\partial \mathbf{B}}{\partial t} \quad (3.2)$$

with the constitutive relations

$$\mathbf{D} = \epsilon_0 \mathbf{E} + \mathbf{P} \quad (3.3)$$

$$\mathbf{B} = \mu_0 (\mathbf{H} + \mathbf{M}) \quad (3.4)$$

Only nonmagnetic materials ($\mathbf{M} = 0$) are considered here. Assuming scalar quantities and taking the curl of Eqn. (3.2), using (3.1) and (3.4) yields:

$$\begin{aligned}
 \nabla \times (\nabla \times E) &= -\frac{\partial}{\partial t}(\nabla \times B) \\
 &= -\mu_0 \frac{\partial}{\partial t}(\nabla \times H) \\
 &= -\mu_0 \frac{\partial}{\partial t} \left(\frac{\partial D}{\partial t} \right) \\
 &= -\mu_0 \epsilon_0 \frac{\partial^2}{\partial t^2} E - \mu_0 \frac{\partial^2}{\partial t^2} P
 \end{aligned} \tag{3.5}$$

The electric polarization can be expressed in terms of linear and nonlinear components as

$$\begin{aligned}
 P &= \epsilon_0 \left(\chi_{\text{Lin}}^{(1)} + \chi^{(2)} E + \chi^{(3)} EE + \dots \right) E \\
 &= \epsilon_0 \chi_{\text{Lin}}^{(1)} E + P^{NL}
 \end{aligned} \tag{3.6}$$

and a vector identity can be used to replace the left side of (3.5) by

$$\nabla \times \nabla \times E = -\nabla^2 E + \nabla (\nabla \cdot E) \tag{3.7}$$

with the assumption that $\nabla \cdot E \approx 0$. The general form of the wave equation with a nonlinear source term can now be written as

$$\nabla^2 E = \mu_0 \epsilon_0 \frac{\partial^2}{\partial t^2} E + \mu_0 \epsilon_0 \chi_{\text{Lin}} \frac{\partial^2}{\partial t^2} E + \mu_0 \frac{\partial^2}{\partial t^2} P^{NL} \tag{3.8}$$

The left side of (3.8) can be written as

$$\begin{aligned}
 \nabla^2 E &= \left(\frac{\partial^2}{\partial x^2} + \frac{\partial^2}{\partial y^2} + \frac{\partial^2}{\partial z^2} \right) E \\
 &= \nabla_{\perp}^2 E + \frac{\partial^2}{\partial z^2} E
 \end{aligned} \tag{3.9}$$

to distinguish the direction of propagation of light (usually assumed to be along z) from the plane of polarization (xy) where

$$\nabla_{\perp}^2 = \frac{\partial^2}{\partial x^2} + \frac{\partial^2}{\partial y^2} \tag{3.10}$$

The complex refractive index, \hat{n} , is related to the linear term of the polarization by

$$\hat{n}^2 = 1 + \chi_{\text{Lin}}^{(1)} \quad (3.11)$$

and the speed of light, c is related to the permittivity, ϵ_0 and magnetic permeability, μ_0 by

$$c^2 = \frac{1}{\mu_0 \epsilon_0} \quad (3.12)$$

Using relations (3.10) through (3.12), (3.8) can be rewritten as

$$\nabla_{\perp}^2 E + \frac{\partial^2 E}{\partial z^2} = \frac{\hat{n}^2}{c^2} \frac{\partial^2 E}{\partial t^2} + \mu_0 \frac{\partial^2}{\partial t^2} P^{NL} \quad (3.13)$$

which is the starting point for the following sections.

In addition, the form of the electric field used here will be:

$$E = A(x, y, z, t) e^{i(k_0 z - \omega t)} + c.c. \quad (3.14)$$

which allows the second term in (3.13) can be written as:

$$\begin{aligned} \frac{\partial^2}{\partial z^2} E &= \frac{\partial^2}{\partial z^2} \left(A(z) e^{i(k_0 z - \omega t)} \right) \\ &= \frac{\partial}{\partial z} \left[A i k_0 e^{i(k_0 z - \omega t)} + \frac{\partial A}{\partial z} e^{i(k_0 z - \omega t)} \right] \\ &= -k_0^2 A e^{i(k_0 z - \omega t)} + 2i k_0 \frac{\partial A}{\partial z} e^{i(k_0 z - \omega t)} + \frac{\partial^2 A}{\partial z^2} e^{i(k_0 z - \omega t)} \end{aligned} \quad (3.15)$$

All the work here involves loosely focused beams where the field amplitude is slowly varying, with respect to the wavelength, along the propagation direction z and the pulse durations are much longer longer then the period of one optical cycle. The allows use of the slowly varying envelope approximations (SVEA) [38]

$$\left| \frac{\partial^2 A}{\partial z^2} \right| \ll \left| k \frac{\partial A}{\partial z} \right| \quad \left| \frac{\partial^2 A}{\partial t^2} \right| \ll \left| \omega \frac{\partial A}{\partial t} \right| \quad (3.16)$$

$$\frac{\partial^2 A}{\partial z^2} \approx 0 \quad \frac{\partial^2 A}{\partial t^2} \approx 0 \quad (3.17)$$

This simplifies (3.15) to

$$\frac{\partial^2}{\partial z^2} E = -k_0^2 A e^{i(k_0 z - \omega t)} + 2ik_0 \frac{\partial A}{\partial z} e^{i(k_0 z - \omega t)} \quad (3.18)$$

and the second order time derivatives of the electric field to

$$\frac{\partial^2}{\partial t^2} E = -\omega_0^2 A e^{i(k_0 z - \omega t)} \quad (3.19)$$

The complex refractive index, \hat{n} , which relates the refractive index and extinction coefficients can be written as [39]

$$\begin{aligned} \hat{n}^2 &= (n + i\kappa)^2 \\ &= n^2 - \kappa^2 + 2i\kappa n \\ &= (n_0 + \Delta n)^2 - (\kappa_0 + \Delta \kappa)^2 + 2i(n_0 + \Delta n)(\kappa_0 + \Delta \kappa) \\ &\approx n_0^2 + 2n_0 \Delta n + 2in_0 \kappa_0 \left(1 + \frac{\Delta \kappa}{\kappa_0}\right) \end{aligned} \quad (3.20)$$

where Δn and $\Delta \kappa$ are perturbations to the refractive index and extinction coefficients respectively.

Since Δn , κ , and $\Delta \kappa$ are small quantities, their second order terms are set to zero. The extinction coefficient κ can be expressed as

$$\kappa_0 = \frac{\alpha_0 \lambda}{4\pi} \quad (3.21)$$

$$\Delta \kappa = \frac{\Delta \alpha \lambda}{4\pi} \quad (3.22)$$

3.3 Wave Equation for Second Order Nonlinearities: Second Harmonic Generation with Walkoff

This section will derive the coupled wave equations for SHG in a Type I medium where

$$o + o \leftrightarrow e$$

$$\lambda_\omega + \lambda_\omega \leftrightarrow \lambda_{2\omega}$$

pump and generated beams polarized as ordinary and extraordinary waves respectively. This is a three wave mixing process where two of the waves are degenerate. By convention, the degenerate field is termed the pump and the field at 2ω is the SHG, or signal, field. In general, the second order term of the nonlinear polarization can be written as:

$$P^{(2)} = \epsilon_0 \chi^{(2)} E^2 \quad (3.23)$$

Using d_{eff} , which is $\frac{1}{2}\chi^{(2)}$, and expressing the fields as in (3.14), the $P^{(2)}$ expressions that will be used in (3.13) are [38]

$$P_{\omega_P}^{(2)} = 4\epsilon_0 d_{\text{eff}} A_P^* A_S \exp(i(\Delta kz - \omega_P t)) \quad (3.24)$$

$$P_{\omega_S}^{(2)} = 2\epsilon_0 d_{\text{eff}} A_P A_P \exp(-i(\Delta kz - \omega_S t)) \quad (3.25)$$

where

$$\Delta k = 2k_P - k_S \quad (3.26)$$

The $P^{(2)}$ terms couple the energy from the pump field, A_P , to the signal field, A_S .

3.3.1 Ordinary Polarized Beam

This section will derive the nonlinear wave equation for the ordinary polarized pump field.

Substituting (3.24) into (3.13) and expressing the electric fields as (3.14) results in

$$\nabla_{\perp}^2 A_P - k_P^2 A_P + 2ik_P \frac{\partial A_P}{\partial z} = -\frac{\hat{n}^2}{c^2} \omega_P^2 A_P - 4\mu_0 \epsilon_0 \omega_P^2 d_{\text{eff}} A_P^* A_S \exp(i\Delta kz) \quad (3.27)$$

Note that:

$$k_0^2 = \left(\frac{2\pi n_0}{\lambda} \right)^2 \quad (3.28)$$

$$= \frac{4\pi^2}{\lambda^2} n_0^2 \quad (3.29)$$

$$= \frac{\omega^2}{c^2} n_0^2 \quad (3.30)$$

and rearranging terms gives

$$\nabla_{\perp}^2 A_P + 2ik_P \frac{\partial A_P}{\partial z} = \frac{\omega_P^2}{c^2} (n_0^2 - \hat{n}^2) A_P - 4 \frac{\omega_P^2 d_{\text{eff}}}{c^2} A_P^* A_S \exp(i\Delta kz) \quad (3.31)$$

Using (3.20) with Δn and $\Delta \kappa = 0$ since no irradiance or thermal induced changes to the refractive index or linear absorption occur (unlike for $\chi^{(3)}$ interactions) the complex refractive index can be written as

$$\hat{n}^2 = n_0^2 + \frac{2in_0\alpha_0\lambda}{4\pi} \quad (3.32)$$

using this in (3.31) produces

$$\begin{aligned} \nabla_{\perp}^2 A_P + 2ik_P \frac{\partial A_P}{\partial z} &= -\frac{\omega_P^2 2in_P \alpha_P \lambda_P}{4\pi c^2} A_P - 4 \frac{\omega_P^2 d_{\text{eff}}}{c^2} A_P^* A_S \exp(i\Delta kz) \\ &= -ik_P \alpha_P A_P - 4 \frac{\omega_P^2 d_{\text{eff}}}{c^2} A_P^* A_S \exp(i\Delta kz) \end{aligned} \quad (3.33)$$

Rearranging terms results in

$$\frac{\partial A_P}{\partial z} = \frac{i}{2k_P} \nabla_{\perp}^2 A_P - \frac{\alpha_P}{2} A_P + \frac{i2d_{\text{eff}}\omega_P}{c n_P} A_P^* A_S \exp(i\Delta kz) \quad (3.34)$$

3.3.2 Extraordinary Polarized Beam with Walkoff

For the extraordinary polarized beam in a birefringent crystal, the Poynting and wave vectors are not collinear but are at an angle ρ with respect to each other. Figure 3.1 shows a schematic of the direction of the Poynting vector along z' at an angle ρ to the z axis. As in the previous section, a similar set of steps can be done to find the nonlinear wave equation for the extraordinary polarized signal beam propagating in the z' direction

$$\frac{\partial A_S}{\partial z'} = \frac{i}{2k_S} \nabla_{\perp}^2 A_S - \frac{\alpha_S}{2} A_S + \frac{id_{\text{eff}}\omega_S}{c n_S} A_P A_P \exp(i\Delta kz) \quad (3.35)$$

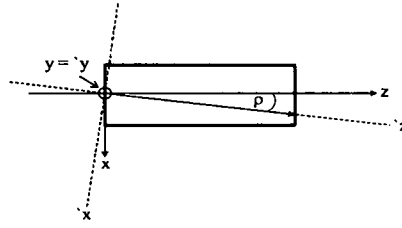


Figure 3.1: Schematic of walk-off direction within crystal and lab reference frame

A coordinate transformation must be done to (3.35) to convert to the lab (xyz) reference frame.

Relationships between the primed and unprimed axis in Fig. 3.1 are

$$x = x' \cos \rho + z' \sin \rho \quad (3.36)$$

$$z = z' \cos \rho - x' \sin \rho \quad (3.37)$$

Relating the derivative along z' direction

$$\begin{aligned} \frac{\partial A}{\partial z'} &= \frac{\partial A}{\partial z} \frac{\partial z}{\partial z'} + \frac{\partial A}{\partial x} \frac{\partial x}{\partial z'} \\ &= \cos(\rho) \frac{\partial A}{\partial z} + \sin(\rho) \frac{\partial A}{\partial x} \end{aligned} \quad (3.38)$$

Rotation in the crystal is about the y' axis such that $y = y'$, therefore

$$\nabla_{\perp}^2 = \frac{\partial^2}{\partial x'^2} + \frac{\partial^2}{\partial y'^2} \quad (3.39)$$

Expanding the second order derivative in x' gives

$$\begin{aligned} \frac{\partial^2 A}{\partial x'^2} &= \frac{\partial}{\partial x'} \left(\frac{\partial A}{\partial x'} \right) \\ &= \frac{\partial}{\partial x} \left(\frac{\partial A}{\partial x'} \right) \frac{\partial x}{\partial x'} + \frac{\partial}{\partial z} \left(\frac{\partial A}{\partial x'} \right) \frac{\partial z}{\partial x'} \end{aligned} \quad (3.40)$$

Finding the field derivative with respect to x' :

$$\begin{aligned} \frac{\partial A}{\partial x'} &= \frac{\partial A}{\partial z} \frac{\partial z}{\partial x'} + \frac{\partial A}{\partial x} \frac{\partial x}{\partial x'} \\ &= -\sin(\rho) \frac{\partial A}{\partial z} + \cos(\rho) \frac{\partial A}{\partial x} \end{aligned} \quad (3.41)$$

and using this in (3.40) produces

$$\begin{aligned} \frac{\partial^2 A}{\partial x'^2} = & \left[-\sin(\rho) \frac{\partial^2 A}{\partial x \partial z} + \cos(\rho) \frac{\partial^2 A}{\partial x^2} \right] \cos(\rho) \\ & - \sin(\rho) \left[-\sin(\rho) \frac{\partial^2 A}{\partial z^2} + \cos(\rho) \frac{\partial^2 A}{\partial x^2} \right] \end{aligned} \quad (3.42)$$

Since ρ is small, the small angle approximation can be used to simplify (3.42) to

$$\frac{\partial^2 A}{\partial x'^2} = \cos^2(\rho) \frac{\partial^2 A}{\partial x^2} \approx \frac{\partial^2 A}{\partial x^2} \quad (3.43)$$

and therefore

$$\nabla_{\perp}^2 = \nabla'_{\perp}{}^2 \quad (3.44)$$

Using (3.38) and (3.44) in (3.35), the wave equation can now be expressed in the lab coordinates as

$$\frac{\partial A_S}{\partial z} \cos(\rho) + \sin(\rho) \frac{\partial A_S}{\partial x} = \frac{1}{2ik_0} \nabla_{\perp}^2 A_S - \frac{\alpha_S}{2} A_S + \frac{i2d_{\text{eff}}\omega_S}{cn_S} A_P A_P \exp(i\Delta kz) \quad (3.45)$$

Rearranging and noting that $\cos(\rho) \approx 1 \approx \frac{1}{\cos(\rho)}$

$$\frac{\partial A_S}{\partial z} = \frac{1}{2ik_0} \nabla_{\perp}^2 A_S - \frac{\sin(\rho)}{\cos(\rho)} \frac{\partial A_S}{\partial x} - \frac{\alpha_S}{2} A_S + \frac{i2d_{\text{eff}}\omega_S}{cn_S} A_P A_P \exp(i\Delta kz) \quad (3.46)$$

The final set of coupled A_P and A_S equations used in Ch. 5 are

$$\frac{\partial A_P}{\partial z} = \frac{i}{2k_P} \nabla_{\perp}^2 A_P + \frac{i2d_{\text{eff}}\omega_P}{cn_P} A_P^* A_S \exp(i(k_S - 2k_P)z) - \frac{\alpha_P}{2} A_P \quad (3.47)$$

$$\frac{\partial A_S}{\partial z} = \frac{i}{2k_S} \nabla_{\perp}^2 A_S - \tan(\rho) \frac{\partial A_S}{\partial x} + \frac{i2d_{\text{eff}}\omega_P}{cn_S} A_P A_P \exp(-i(k_S - 2k_P)z) - \frac{\alpha_S}{2} A_S \quad (3.48)$$

3.4 Third Order Optical Nonlinearities in Semiconductors

3.4.1 Wave Equation with Bound Electronic, Free Carrier and Thermal Nonlinearities

This section derives the wave equation in a $\chi^{(3)}$ medium where two photon absorption and nonlinear refraction are present. In addition, the effects of free carrier and thermal nonlinearities

are included. The interactions to be investigated are third order nonlinearities involving a single frequency of light. Therefore, the nonlinear polarization of interest is:

$$P^{NL} = \epsilon_0 \chi^{(3)} |E|^2 E \quad (3.49)$$

and Eqn. (3.13) can be rewritten as:

$$\nabla_{\perp}^2 A + 2ik_o \frac{\partial A}{\partial z} = k_o^2 A - \frac{\omega^2}{c^2} \left(1 + \chi_{\text{Lin}}^{(1)} \right) A - \frac{\omega^2}{c^2} \chi^{(3)} |A|^2 A \quad (3.50)$$

As with SHG, replacing the linear susceptibility, $\chi_{\text{Lin}}^{(1)}$ with the complex refractive index, \hat{n} allows (3.50) to be expressed as:

$$\nabla_{\perp}^2 A + 2ik_o \frac{\partial A}{\partial z} = \frac{\omega^2}{c^2} (n_0^2 - \hat{n}^2) A - \frac{\omega^2}{c^2} \chi^{(3)} |A|^2 A \quad (3.51)$$

and using Eq. (3.20) in (3.51)

$$\frac{\partial A}{\partial z} = -\frac{1}{2ik_o} \nabla_{\perp}^2 A - \frac{\omega^2}{c^2 2ik_o} \left[2n_0 \Delta n + 2in_0 \kappa_0 \left(1 + \frac{\Delta \kappa}{\kappa_0} \right) \right] A - \frac{\omega^2}{c^2 2ik_o} \chi^{(3)} |A|^2 A \quad (3.52)$$

noting that

$$\frac{\omega^2}{c^2 2ik_o} = -\frac{i\pi}{\lambda n_0} \quad (3.53)$$

and after some additional manipulations, the wave equation can now be written as:

$$\frac{\partial A}{\partial z} = \frac{i}{2k_o} \nabla_{\perp}^2 A - \frac{2\pi}{\lambda} (i\Delta n - \kappa_0 - \Delta \kappa) A - \frac{i\pi}{\lambda n_0} \chi^{(3)} |A|^2 A \quad (3.54)$$

Using the definition of the extinction coefficient

$$\frac{\partial A}{\partial z} = \frac{i}{2k_o} \nabla_{\perp}^2 A - \left[\frac{2i\pi \Delta n}{\lambda} - \frac{\alpha_0}{2} - \frac{\Delta \alpha}{2} \right] A - \frac{i\pi}{\lambda n_0} \chi^{(3)} |A|^2 A \quad (3.55)$$

In S.I. units, the complex third order polarization can be expressed as [38]:

$$\chi^{(3)} = \epsilon_0 n_0^2 c \left(4\gamma + \frac{i\lambda\beta}{\pi} \right) \quad (3.56)$$

here γ is the instantaneous, bound electronic, irradiance dependent change in refractive index. The units of γ are $\frac{cm^2}{W}$. Some references refer to this term as n_2 , however in this dissertation, n_2 is reserved for units of *esu*. Based on the definition of the electric field given in Eq. (3.14), the corresponding irradiance is:

$$I = 2n_0\epsilon_0c|A|^2 \quad (3.57)$$

and using these definitions of irradiance and third order susceptibility in Eq. (3.55), the final form of the nonlinear wave equation for $\chi^{(3)}$ interactions which will be used throughout this dissertation is:

$$\frac{\partial A}{\partial z} = \frac{i}{2k_0} \nabla_{\perp}^2 A + \frac{2i\pi}{\lambda} (\Delta n + \gamma I) A - (\alpha_0 + \Delta\alpha + \beta I) \frac{A}{2} \quad (3.58)$$

Here the change in refractive index, Δn , arises from free carrier and thermal effects. Acoustic and/or electro-optic effects could also be included but are not addressed here. The refractive index change is expressed as

$$\Delta n = \frac{dn}{dN} N + \frac{dn}{dT} \Delta T \quad (3.59)$$

$$= \sigma_{ref} N + \frac{dn}{dT} \Delta T \quad (3.60)$$

to avoid ambiguity, the term $\frac{dn}{dN}$ is written as σ_{ref} . The parameters N and ΔT are the generated free carriers and temperature rise which occur during the optical pulse. The change in absorption, $\Delta\alpha$, is due to free carriers generated during the optical pulse

$$\Delta\alpha = \sigma_{abs} N \quad (3.61)$$

where σ_{abs} is the free carrier absorption cross section. Equation (3.58) can also be rewritten in the more familiar form

$$\frac{dI}{dz} = -(\alpha + \sigma_{abs} N) I - \beta I^2 \quad (3.62)$$

3.4.2 Charge Carrier Generation

As light is absorbed in a semiconductor, both linearly and nonlinearly, e-h pairs are created generating free charge carriers. The carrier generation equation is given as[40]:

$$\begin{aligned} \frac{\partial N}{\partial t} &= \text{Diffusion} & + & & \text{Generation} & - & \text{Recombination} \\ &= \nabla (D \nabla N) & + & & \frac{\alpha I}{h\nu} + \frac{\beta I^2}{2h\nu} & - & \frac{N}{\tau} \end{aligned} \quad (3.63)$$

For the time scales here, diffusion effects can be ignored. This has been experimentally verified and is discussed in Ch. 6. With diffusion removed, the carrier generation rate equation used here is:

$$\frac{\partial N}{\partial t} = \frac{\alpha I}{h\nu} + \frac{\beta I^2}{2h\nu} - \frac{N}{\tau} \quad (3.64)$$

3.4.3 Heat Equation

The full expression for the nonsteady state heat equation with a source term is given below [41]

$$\begin{aligned} \rho c \frac{\partial \Delta T}{\partial t} &= \text{Diffusion} & + & & \text{Generation} \\ &= k \nabla^2 (\Delta T) & + & & ((\alpha + \sigma_{\text{abs}} N) I + \beta I^2) \end{aligned} \quad (3.65)$$

Thermal diffusion occurs on a much longer time scale then the pulse durations considered here, therefore the form of the heat equation used is

$$\frac{\partial \Delta T}{\partial t} = \frac{1}{\rho c} ((\alpha + \sigma_{\text{abs}} N) I + \beta I^2) \quad (3.66)$$

CHAPTER IV

NUMERICAL METHOD

4.1 Introduction

This chapter covers the numerical methods used throughout the dissertation. All methods are based on splitting of the linear and nonlinear operations in order to solve them independently. Linear propagation equation is solved through the use of Fast Fourier Transforms (FFTs) to solve the paraxial wave equation. Propagation through a medium with second and third order nonlinearities is solved through use of finite difference approximations assuming no diffraction of the beam. Phase retrieval uses a combination of FFTs to propagate the fields and a predictor-corrector algorithm to extract the phase information.

The numerical model developed to analyze second and third order nonlinear optical interactions is four dimensional in nature, which can accommodate a complex electro-magnetic field $A(x, y, z, t)$ of arbitrary spatial and temporal shape (for pulses longer than 100 fs in duration). Analytic and arbitrary spatial, phase and temporal profiles can be entered into the model. The model can also take as inputs the experimental transverse spatial distribution found either by use of a camera or through a pinhole raster scan. For ns and longer duration pulses, the temporal profile is recorded with a fast photodiode and oscilloscope and can be entered in the model after proper normalization. The normalization factor is determined from the measurement of the incident energy and using the

actual spatial and temporal profiles. The only assumptions made in the nonlinear wave equations are:

1. Slowly varying envelope/paraxial approximation is made

$$\begin{aligned}\frac{\partial^2 A}{\partial z^2} &\ll k \frac{\partial A}{\partial z} \\ \frac{\partial^2 A}{\partial z^2} &\approx 0\end{aligned}$$

2. Single frequency, quasi-monochromatic light. The treatment here is not completely valid for ultrafast pulses of large bandwidths (i.e. valid for pulsewidths < 100 fs).

3. No time dependence to the phase

$$A = \text{Amp}(x, y, z, t) \exp(i\phi(x, y, z))$$

4.2 $\chi^{(2)}$ Second Harmonic Generation

Second harmonic generation (SHG) can be expressed as a pair of coupled partial differential equations. For the case of a Type I interactions between an o-polarized pump field (A_P) which generates an e-polarized signal (A_S) that experiences walk-off, the coupled wave equations can be written as:

$$\frac{\partial A_P}{\partial z} = \frac{i}{2k_P} \nabla_{\perp}^2 A_P + \frac{i2d_{\text{eff}}\omega_P}{cn_P} A_P^* A_S \exp(i(k_S - 2k_P)z) - \frac{\alpha_P}{2} A_P \quad (4.1)$$

$$\begin{aligned}\frac{\partial A_S}{\partial z} &= \frac{i}{2k_S} \nabla_{\perp}^2 A_S - \tan(\rho) \frac{\partial A_S}{\partial x} \\ &\quad + \frac{i2d_{\text{eff}}\omega_P}{cn_S} A_P A_P \exp(-i(k_S - 2k_P)z) - \frac{\alpha_S}{2} A_S\end{aligned} \quad (4.2)$$

To determine an analytic solutions of (4.1) and (4.2) some assumptions such as having collimated beams ($\nabla_{\perp}^2 = 0$) or no pump depletion, ($dA_P/dz = 0$) are typically made. For a general

solution with no assumptions and which can handle arbitrary spatial and temporal profiles, numerical methods must be used, for which a variety of approaches exist. A finite difference method can be applied to (4.1) and (4.2) which will require solution of a system of linear equations. Another numerical technique is the split-step method where the right side of Eq. (4.1) and (4.2) are separated into different operations, one for propagation and a second for absorption and nonlinearities. This allows each operator to be solved independently and is the method that will be used here. A similar method is used in [42].

The split step method for SHG used here is as follows. Expressing (4.1) in terms of propagation and nonlinear operators:

$$\frac{\partial A_P}{\partial z} = \frac{i}{2k_p} \nabla_{\perp}^2 A_P + \frac{i2d_{\text{eff}}\omega_P}{cn_P} A_P^* A_S \exp(i(k_S - 2k_P)z) - \frac{\alpha_P}{2} A_P \quad (4.3)$$

$$= \widehat{P}A_P + \widehat{NL} \quad (4.4)$$

where

$$\widehat{P} = \frac{i}{2k_p} \nabla_{\perp}^2 \quad (4.5)$$

$$\widehat{NL} = \frac{i2d_{\text{eff}}\omega_P}{cn_P} A_P^* A_S \exp(i(k_S - 2k_P)z) - \frac{\alpha_P}{2} A_P \quad (4.6)$$

In general, solution of Eq. (4.4) is as follows. The sample is divided into N slices, each of length Δz . Propagation over each Δz involves the following steps:

1. Based on the incident energy and spatial and temporal beam profiles, determine the incident pump field, $A_P(x, y, z = 0, t)$ just inside the front surface (i.e., taking into account the transmission coefficient).
2. Set the initial signal field $A_S(x, y, z = 0, t) = 0$.
3. Set $\widehat{NL} = 0$ and propagate the fields using \widehat{P} for a distance Δz .

4. Set $\hat{P} = 0$ and solve Eq. (4.4) with only the \widehat{NL} part using finite difference techniques to determine A_P and A_S .
5. The A_p and A_s fields become to inputs to the next ΔZ slice
6. Repeat 3, 4 & 5 until fields propagate to the end of the crystal
7. Calculate the field outside the crystal with the appropriate transmission coefficient.
8. Calculate the pump and signal irradiances, $I_{P,S}(x, y, z = l, t)$ just after the exit face by squaring the field amplitudes.
9. Spatially and temporally integrate the irradiances to determine the output pump and signal energies.

Next two sections will discuss the numerical methods used to solve Eq. (4.4).

4.2.1 Solution of the \hat{P} Operator

The propagation operator equation will be solved in the spatial frequency domain via the use of fast Fourier Transforms (FFT's). The definition of a 2-dimensional Fourier Transform, \mathfrak{F} , of a complex array A as given in [43]:

$$\mathfrak{F}(A(x, y)) = \tilde{A}(x, y) = \iint A(x, y) \exp(-i2\pi(f_x x + f_y y)) dx dy \quad (4.7)$$

Setting $\widehat{NL} = 0$ in (4.4) gives

$$\frac{\partial A_P}{\partial z} = \hat{P} A_p \quad (4.8)$$

Taking the Fourier transform of each side yields:

$$\frac{\partial \tilde{A}_P}{\partial z} = \hat{P} \tilde{A}_p \quad (4.9)$$

applying \hat{P} from (4.5) to \tilde{A}_P :

$$\begin{aligned}\frac{\partial \tilde{A}_P}{\partial z} &= \frac{i}{2k_p} (-4\pi^2 (f_x^2 + f_y^2)) \tilde{A}_P \\ &= \frac{-i\pi\lambda_p}{n_p} (f_x^2 + f_y^2) \tilde{A}_P\end{aligned}\quad (4.10)$$

solving for the field at $z + \Delta z$:

$$\tilde{A}_P(z + \Delta z) = \exp\left(\frac{-i\pi\lambda_p\Delta z}{n_p} (f_x^2 + f_y^2)\right) \tilde{A}_P(z) \quad (4.11)$$

Taking the inverse Fourier transform to retrieve the field in real space yields

$$\begin{aligned}A_P(z + \Delta z) &= \mathfrak{F}^{-1} \left[\exp\left(\frac{-i\pi\lambda_p\Delta z}{n_p} (f_x^2 + f_y^2)\right) \tilde{A}_P(z) \right] \\ &= \mathfrak{F}^{-1} \left[\exp\left(\frac{-i\pi\lambda_p\Delta z}{n_p} (f_x^2 + f_y^2)\right) \mathfrak{F}(A_P(z)) \right]\end{aligned}\quad (4.12)$$

Equation (4.12) is solved numerically using FFTs in the following steps:

1. Take the discrete Fourier transform of $A_P(z)$ via an FFT to get $\tilde{A}_P(z)$
2. Find $\tilde{A}_P(z + \Delta z) = \tilde{A}_P(z) \exp\left(\frac{-i\pi\lambda_p\Delta z}{n_p} (f_x^2 + f_y^2)\right)$
3. Take the IFFT of the $\tilde{A}_P(z + \Delta z)$ to get $A_P(z + \Delta z)$

Note that for the e-polarized signal field which experiences walk-off, \hat{P} becomes

$$\hat{P} = \frac{i}{2k_p} \nabla_{\perp}^2 - \tan(\rho) \frac{\partial}{\partial x} \quad (4.13)$$

and following a similar set of steps the A_S can be found by

$$A_S(z + \Delta z) = \mathfrak{F}^{-1} \left[\exp\left(\frac{-i\pi\lambda_p\Delta z}{n_S(\theta)} (f_x^2 + f_y^2) - \frac{\pi f_x \tan(\rho)}{k_S}\right) \mathfrak{F}(A_S(z)) \right] \quad (4.14)$$

4.2.2 Solution of the \widehat{NL} Operator

Setting $\widehat{P} = 0$ the coupled SHG equations are:

$$\frac{\partial A_P}{\partial z} = \frac{i2d_{\text{eff}}\omega_P}{cn_P} A_P^* A_S \exp(i(k_S - 2k_P)z) - \frac{\alpha_P}{2} A_P \quad (4.15)$$

$$\frac{\partial A_S}{\partial z} = \frac{i2d_{\text{eff}}\omega_P}{cn_S} A_P A_P \exp(-i(k_S - 2k_P)z) - \frac{\alpha_S}{2} A_S \quad (4.16)$$

These are solved using implicit, forward finite difference approximations. The initial conditions are that $A_P(x, y, z = 0, t)$ is known and $A_S(x, y, z = 0, t) = 0$, therefore Eq. (4.16) is solved first.

Expressing Eq. (4.16) as a finite difference equation gives:

$$\frac{A_S^{z+\Delta z} - A_S^z}{\Delta z} = C_s A_P^{z+\Delta z} A_P^{z+\Delta z} - \frac{\alpha_S}{2} A_S^{z+\Delta z} \quad (4.17)$$

where C_s is a collection of constants given as

$$C_s = \frac{i2d_{\text{eff}}\omega_P}{cn_S} \exp(-i(k_S - 2k_P)z) \quad (4.18)$$

and solving for $A_S(z + \Delta z)$ gives:

$$A_S^{z+\Delta z} = \frac{A_S^z + \Delta z C_s A_P^{z+\Delta z} A_P^{z+\Delta z}}{1 + \Delta z \frac{\alpha_S}{2}} \quad (4.19)$$

Having generated the signal field the pump field experiences depletion through the nonlinear interaction. In a similar manner to the signal field, the finite difference expression for the pump field, $A_P(z + \Delta z)$ is

$$A_P^{z+\Delta z} = \frac{A_P^z + \Delta z C_p A_P^{*,z} A_S^{z+\Delta z}}{1 + \Delta z \frac{\alpha_P}{2}} \quad (4.20)$$

To model the SHG process, as is done in Ch. 5, the following procedure was used. First each time slice of A_P and A_S was propagated using (4.12) and (4.14) a distance Δz . Next (4.19) and (4.20) were used to update the fields due to the nonlinear coupling. These updated fields become

the new initial conditions to the next Δz slice. This process was repeated until the fields reached the crystal exit. At the output face of the crystal, the field irradiances were found. The irradiances were then temporally and spatially integrated to determine the output energies.

The number of Δz steps through the crystal was determined via a numerical experiment. At the largest incident irradiance value, the program was run with an increasing number of steps. The output energy of the signal field was then plotted as a function of the number of Δz steps. Once the change in output energy was below a chosen tolerance level, the associated number of Δz steps was recorded and used for all analysis.

4.3 $\chi^{(3)}$ Nonlinear Absorption and Refraction

The nonlinear wave equation describing propagation of a complex electro-magnetic field $A(x, y, z, t)$ through a $\chi^{(3)}$ medium as derived in Ch. 3 is

$$\frac{\partial A}{\partial z} = \frac{i}{2k_0} \nabla_{\perp}^2 A + \frac{2i\pi}{\lambda} \left(\sigma_{\text{ref}} N + \frac{dn}{dT} \Delta T + \gamma I \right) A - (\alpha + \sigma_{\text{abs}} N + \beta I) \frac{A}{2} \quad (4.21)$$

with the coupled equations specifying free carrier generation, $N(x, y, t)$, and heat rise, $\Delta T(x, y, t)$ given as:

$$\frac{\partial N}{\partial t} = \frac{\alpha I}{h\nu} + \frac{\beta I^2}{2h\nu} - \frac{N}{\tau} \quad (4.22)$$

$$\frac{\partial \Delta T}{\partial t} = \frac{1}{\rho c} [(\alpha + \sigma_{\text{abs}} N) I + \beta I^2] \quad (4.23)$$

Equation (4.21) is similar to (4.1) and (4.2) in that the field along the propagation direction is a function of diffraction and nonlinearities. In a similar manner to the SHG analysis, this can be expressed using operator notation as:

$$\frac{\partial A}{\partial z} = \left[\hat{P} + \widehat{NL} \right] A \quad (4.24)$$

where the diffraction operation, \widehat{P} is the same as (4.5) and \widehat{NL} is given as:

$$\widehat{NL} = \frac{2i\pi}{\lambda} \left(\sigma_{\text{ref}} N + \frac{dn}{dT} \Delta T + \gamma I \right) - \frac{1}{2} (\alpha + \sigma_{\text{abs}} N + \beta I) \quad (4.25)$$

As before with SHG, since \widehat{P} and \widehat{NL} occur simultaneously it is difficult to find analytic solutions. Early numerical modeling used a finite difference method assuming radially symmetric beams and ignoring diffraction effects (i.e. thin sample approximation). Some of this work was presented at the 6th International Congress on Industrial and Applied Mathematics and was published in [5].

In order to have a more general solution with minimal assumptions and which can handle arbitrary beam shapes, the split step numerical method is used here. The split step method gives an approximate solution to the nonlinear wave equation by treating the \widehat{P} and \widehat{NL} operators independently. In other words, the assumption has been made that \widehat{P} and \widehat{NL} are noncommutative. An additional assumption is that both of these operators are not functions of the z coordinate, which is true for small enough Δz .

Here the solution of (4.24) is treated differently from (4.4). Solving (4.24) for the field A_1 a distance Δz from the known field A_0 gives

$$\int_z^{z+\Delta z} \frac{\partial A}{A} = \int_z^{z+\Delta z} [\widehat{P} + \widehat{NL}] \partial z \quad (4.26)$$

$$\log \left(\frac{A_1}{A_0} \right) = [\widehat{P} + \widehat{NL}] \Delta z \quad (4.27)$$

$$A_1(z + \Delta z) \approx \exp(\widehat{P}\Delta z) \exp(\widehat{NL}\Delta z) A_0(z) \quad (4.28)$$

The approximation in (4.28) arises from use of the Baker-Campbell-Hausdorff (BCH) formula [44] for two noncommutative operators, \hat{a} , \hat{b} :

$$\exp(\hat{a}) \exp(\hat{b}) = \exp \left(\hat{a} + \hat{b} + \frac{1}{2} [\hat{a}, \hat{b}] + \dots \right) \quad (4.29)$$

Setting $\hat{a} = \Delta z \hat{P}$ and $\hat{b} = \Delta z \widehat{NL}$ the error due to truncation is of second order, $\mathcal{O}(\Delta z^2)$. Accuracy can be improved to second order and error can be improved to order $\mathcal{O}(\Delta z^3)$ by modification of Eq. (4.28) using Strang splitting to split one of the operators into two half-steps. Either operator, \hat{P} or \widehat{NL} , can be chosen. Here the diffraction operator is chosen. Using Strang splitting this is shown as:

$$A_1 \approx \exp\left(\hat{P}\frac{\Delta z}{2}\right) \exp\left(\widehat{NL}\Delta z\right) \exp\left(\hat{P}\frac{\Delta z}{2}\right) A_0 \quad (4.30)$$

The reduction in error using BCH can be seen by application of (4.29) to (4.30) twice, first:

$$\exp\left(\hat{P}\frac{\Delta z}{2}\right) \exp\left(\widehat{NL}\Delta z\right) = \exp\left(\hat{P}\frac{\Delta z}{2} + \widehat{NL}\Delta z + \frac{1}{2}\Delta z^2 \left[\frac{\hat{P}}{2}, \widehat{NL}\right] + \dots\right) \quad (4.31)$$

and then multiplying the result in (4.31) by $\exp\left(\hat{P}\frac{\Delta z}{2}\right)$ yields:

$$\exp\left(2\hat{P}\frac{\Delta z}{2} + \widehat{NL}\Delta z + \frac{1}{2}\Delta z^3 \left[\frac{\hat{P}}{2}\widehat{NL}, \frac{\hat{P}}{2}\right] + \dots\right) \quad (4.32)$$

where the truncation error is now of order $\mathcal{O}(\Delta z^3)$. In general, the numerical solution of Eq. (4.21) using (4.30) can be obtained from the following procedure.

1. Based on the incident energy and spatial and temporal beam profiles, determine the incident field, $A(x, y, z = 0, t)$ just inside the front surface taking into account transmission losses.
2. Propagate each time slice of the field a distance $\frac{\Delta z}{2}$.
3. Calculate the irradiance, $I(x, y, t)$, for each $A(x, y, z = \frac{\Delta z}{2}, t)$.
4. Use $I(x, y, t)$ to solve the $\frac{\partial N}{\partial t}$ rate equation for $N(x, y, t)$.
5. Use $I(x, y, t)$ and $N(x, y, t)$ to solve the $\frac{\partial \Delta T}{\partial t}$ rate equation for $\Delta T(x, y, t)$.
6. With $N(x, y, t)$ and $\Delta T(x, y, t)$ calculated, apply the \widehat{NL} to each $A(x, y, z = \frac{\Delta z}{2}, t)$.
7. Propagate the remaining $\frac{\Delta z}{2}$.

8. Repeat 3 - 7 until the end of the crystal is reached.
9. Find the field just outside the sample, taking into account transmission losses.
10. Spatially and temporally integrate $I(x, y, t)$ at the sample exit face to calculate the output energy in order determine the nonlinear absorption.
11. Propagate the field from the exit face to the detector plane and temporally integrate to determine the two dimensional beam profile due to nonlinear refraction.

This procedure is similar to that used by [45] for modeling of Z -scan experiments, except here the sample position is kept fixed at focus and the detector is placed in the near field. Numerical solutions of \hat{P} and \widehat{NL} will be discussed in the following sections.

4.3.1 Solution of the \hat{P} operator

Solution of \hat{P} is the similar to (4.12) where the basic procedure is to apply an FFT, multiply by the exponential phase due to the propagation distance and then an inverse FFT (IFFT) to return back to real space. However, the step size is now $\frac{\Delta z}{2}$. Therefore for M steps through the sample there are now $2M$ propagation operations and $3M$ total operations when \widehat{NL} is included.

In practice the inner half steps can be grouped together making the algorithm more efficient. This can be seen as follows [44], for propagation over a crystal with three slices the algorithm is:

$$\hat{P}_{\frac{1}{2}} \widehat{NL} \hat{P}_{\frac{1}{2}} \hat{P}_{\frac{1}{2}} \widehat{NL} \hat{P}_{\frac{1}{2}} \hat{P}_{\frac{1}{2}} \widehat{NL} \hat{P}_{\frac{1}{2}} \quad (4.33)$$

By grouping the inner $\hat{P}_{\frac{1}{2}}$ operators together the sequence becomes:

$$\hat{P}_{\frac{1}{2}} \widehat{NL} \widehat{P} \widehat{NL} \widehat{P} \widehat{NL} \widehat{P} \widehat{P}_{-\frac{1}{2}} \quad (4.34)$$

The total number of operations have been reduced from $3M$ to $2M + 1$. For small steps sizes this is non critical, however if the total number of steps is 100 then grouping the half step propagation operations reduces the number of operator calculations by one third while keeping the same accuracy.

4.3.2 Solution of the \widehat{NL} operator

Solution of \widehat{NL} requires solution of $N(x, y, t)$ and $\Delta T(x, y, t)$ at the appropriate z location. This is determined by use of an implicit, forward finite difference approximation for (4.22) and (4.23). Expressing the free carrier generation equation as a finite difference gives

$$\frac{N_{t+1} - N_t}{\Delta t} = \frac{\alpha I_{t+1}}{h\nu} + \frac{\beta I_{t+1}^2}{2h\nu} - \frac{N_{t+1}}{\tau} \quad (4.35)$$

Rearranging terms and solving for N_{t+1} gives:

$$N_{t+1} = \frac{1}{1 + \frac{\Delta t}{\tau}} \left[N_t + \frac{\alpha \Delta t I_{t+1}}{h\nu} + \frac{\beta \Delta t I_{t+1}^2}{2h\nu} \right] \quad (4.36)$$

In a similar manner the heat rise due to nonlinear absorption can be expressed in terms of a finite difference as

$$\Delta T_{t+1} = \Delta T_t + \frac{\Delta t}{\rho c} [(\alpha + \sigma_{\text{abs}} N_{t+1}) I_{t+1} + \beta I_{t+1}^2] \quad (4.37)$$

Once $N(x, y, t)$ and $\Delta T(x, y, t)$ have been found the nonlinearities can be applied to the field by

$$A = A \exp(\widehat{NL} \Delta z) \quad (4.38)$$

Note that in some of the work in Ch. 6, β and σ_{abs} are functions of total temperature which is found by:

$$T_{\text{total}}(x, y, t) = T_{\text{initial}} + \Delta T(x, y, t) \quad (4.39)$$

In addition, β is also dependent on the total charge carrier density

$$N_{\text{total}}(x, y, t) = N_0 + N(x, y, t) \quad (4.40)$$

For characterization of nonlinear absorption, knowledge of the incident phase is non-critical for beams which are weakly diverging through the sample. However, for characterization of nonlinear refraction, accurate phase information is necessary in order to properly model propagation of the beam beyond the sample. The next section describes the method used here to numerically retrieve the phase information.

4.4 Phase Retrieval

In order to accurately model a complex electro-magnetic field, especially through a $\chi^{(3)}$ medium where nonlinear refraction is present, both the spatial amplitude and phase distributions of the incident beam must be known. For beams which propagate as a circularly symmetric, TEM_{00} modes, simple expressions exist for describing the phase. In practice, few beams from a laser, especially those generated from a nonlinear process (e.g. OPO, SHG) are truly single mode. This is even more true for high energy pulsed lasers. The beams inside the resonator are usually multi-mode or the resonator is designed such that a flat top amplitude profile is resonated in order to lower the peak fluence inside the cavity while maximizing energy extraction. This prevents damage to the optical components inside the resonator, however the propagating beam is non-Gaussian.

For beams which are non-ideal, a simple method to recover the phase distribution has been developed and implemented. It is based on the work in [46] and more recently [47]. Here the method is slightly altered by use of discrete wavelet transforms (DWT) to aide in noise suppression. In brief, a camera is used to record the beam distribution through the experimental region of interest. Multiple images (typically 4 or 5) are usually recorded at different values of the propagation distance

z , although only two images are sufficient for phase retrieval. When used with an I -scan method for characterization of NLA and NLR, the two planes are chosen to be the sample input plane and the detector plane.

These images are defined as Irrad1 and Irrad2, separated by a distance z_{prop} where propagation from Irrad1 to Irrad2 is in the positive Z direction. The images are background corrected and at each z position, multiple frames are averaged. The pixel counts over the entire captured images should be well below saturation such that a linear camera response is assured over the entire propagation distance. The captured image provides the fluence distribution of the beam with each pixel temporally integrating the beam irradiance at that location. Since each pixel also has a finite area, each pixel count can be correlated with an energy value. For pixel sizes small compared to the beam variation, the pixel count is proportional to the beam irradiance I . Since I is proportional to $|A|^2$, the square root of the pixel count is proportional to the field amplitude, with the phase of the field undetermined.

To determine the spatial distribution of the phase, the following iterative procedure is used. For an irradiance I_1 , an initial guess of the phase is made, which is typically chosen to be zero. Next, the complex electric field at plane 1 is defined as

$$A_1(x, y) = Amp_1(x, y) e^{iPhase_1(x, y)} \quad (4.41)$$

where $Amp_1(x, y)$ is $\sqrt{Irrad1}$. Using Eqn. (4.12), A_1 is propagated a distance z_{prop} to find A_2 . The amplitude and phase of the complex field A_2 are separated and the amplitude is replaced with the original Irrad2 amplitude distribution. A discrete wavelet transform (DWT) is applied to the phase array in order to smooth out the numerical result and decrease the influence of noise. Field A_2 is then propagated $-z_{prop}$ back to the start plane. As before, the amplitude and phase are

separated, the amplitude is replaced with the original Amp_1 and a DWT is reapplied to the phase. The updated A_1 is then propagated z_{prop} and the process is repeated. This procedure is a basic predictor-corrector technique and has been extensively used in the literature [48], [49]. Round trip propagation between the two planes is typically done for between 25 to 100 iterations. To verify that the phase is converging to a solution, the relative error between the phase at plane 1 after each round trip is plotted as a function of the number of round trips.

As an initial verification of the method, the beam from an Nd:YAG laser was apertured and focused by a lens. This created an Airy beam profile at focus, which has a non-trivial phase profile. A FLIR Systems InGaAs camera was used to capture the beam images through focus. The camera array was 320 x 256 with a pixel pitch of 30 μm . The beam focus was located at a distance (z) of 53 cm from the lens. Images for phase retrieval were chosen prior to focus at $z = 10$ and 14 cm with the phase retrieved at $z = 10$ cm. Beam images and the numerically retrieved phase are shown in Fig. 4.1.

Once the phase was retrieved, a complex field was created at $z = 10\text{cm}$ and was propagated to focus at $z = 54\text{cm}$. The beam irradiance was then calculated and this, along with the actual beam image are shown in Fig. 4.2. Figure 4.3 shows the line profiles along the horizontal centers of the actual and numerical beam irradiances. Good agreement is found in the irradiance profiles verifying that the phase information has been accurately retrieved.

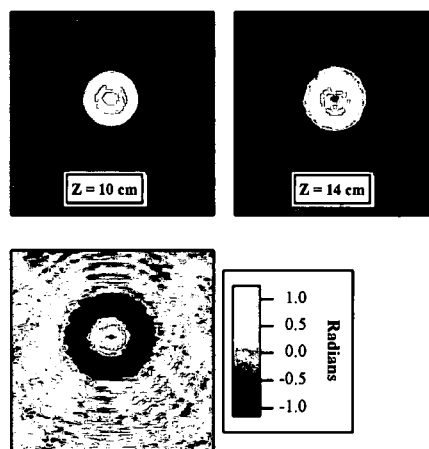


Figure 4.1: Beam images used for phase retrieval at $Z = 10$ and 14 cm. Bottom image is the numerically retrieved phase at $Z = 10$ cm. All images are $4 \times 4 \text{ mm}^2$.

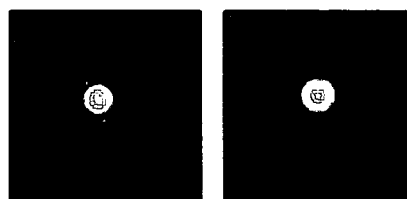


Figure 4.2: Beam images at $Z = 54$ cm. Actual beam image (left) and numerical result (right) are shown. Images are $4 \times 4 \text{ mm}^2$.

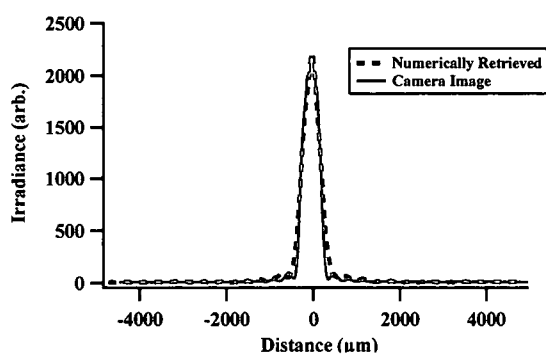


Figure 4.3: Horizontal slice through the centers of the actual camera image at $z = 54$ cm (red) and the numerical result at $z = 54$ cm after propagation of the amplitude and phase information found at $z = 10$ cm

CHAPTER V

APPLICATION OF BEAM PROPAGATION MODELING TO SECOND HARMONIC GENERATION IN CdSiP₂

5.1 Introduction

This chapter is based on the work presented at the 2009 Photonics West conference and published in SPIE proceedings, [6].

A new nonlinear optical crystal, CdSiP₂, recently grown by BAE scientists is an excellent candidate for infrared generation applications because of its thermal properties and ability to phase-match over a large range of wavelengths. Large, high quality, single crystalline samples have recently been grown with transparency from 0.56 to beyond 6 μm . CdSiP₂ has the potential to be pumped at near infrared wavelengths to generate output in the mid and long wave infrared.

5.2 Optical Properties

The refractive index measurements on a CdSiP₂ prism have been presented [50] with the results repeated here. The Sellmeier expressions for light polarized along the ordinary and extraordinary axis are given as:

$$n_o = \sqrt{2.931 + \frac{6.4248\lambda^2}{\lambda^2 - 0.1028} - 0.0032817\lambda^2} \quad (5.1)$$

$$n_e = \sqrt{3.4975 + \frac{5.5451\lambda^2}{\lambda^2 - 0.11713} - 0.0031242\lambda^2} \quad (5.2)$$

From these expressions it is seen that CdSiP_2 is a negative uniaxial material ($n_o > n_e$). Based on these Sellmeier expressions, a phase-matching curve for a Type I interaction vs. angle is shown in Fig. 5.1. For the phase-matching graph, the highest frequency light at (ω_1) was held fixed ($\lambda_1 = 2.39 \mu\text{m}$) and the lower frequency signal (ω_2) and idler (ω_3) were allowed to vary. Degeneracy for the signal and idler wavelengths ($\lambda_2 = \lambda_3 = 4.78 \mu\text{m}$) is predicted at an angle of $\theta = 42.31^\circ$. The crystal used in this testing was cut at an angle of $\theta = 42.5^\circ$, a difference of 0.19° internally or 0.56° in air.

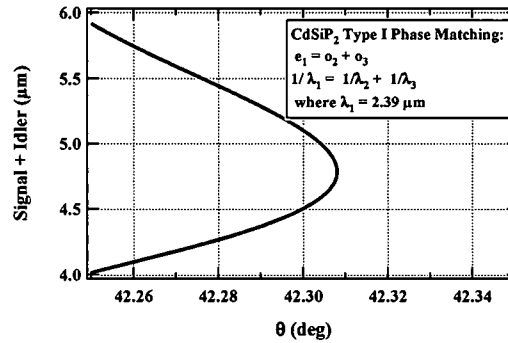


Figure 5.1: Theoretical Type I ($e_1 \leftrightarrow o_2 + o_3$) phase-matching plot for CdSiP_2 at a wavelength of $\lambda_1 = 2.39 \mu\text{m}$. Second harmonic generation is predicted at an angle of $\theta = 42.31^\circ$

The CdSiP_2 crystal (sample 11B) used for testing was fabricated with dimensions of $3.7 \times 7.0 \times 11.7 \text{ mm}^3$ and was uncoated. A picture of the crystal is shown in Fig. 5.2. Walk-off for the e-polarized light at an angle of 42.31° is 16.8 mrad . Over the 11.7 mm interaction length, this caused $197 \mu\text{m}$ of translation of the SHG beam. At the phase-matching angle, $n(\lambda_{2,3}) = n(\lambda_1, \theta) = 3.0512$, giving a Fresnel reflectance of 25.6% per surface. Linear absorption measurements on a sister sample (9A) from the same boule are presented in Figure 5.3. Linear absorption values are

0.25 cm^{-1} at $2.39 \mu\text{m}$, e-polarization and 0.001 cm^{-1} at $4.78 \mu\text{m}$, o-polarization. Bulk absorption loss at $2.39 \mu\text{m}$ for sample 11B is 25%.

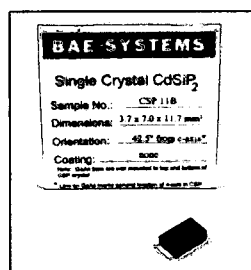


Figure 5.2: Image of CdSiP_2 crystal 11B used for second harmonic generation experiments

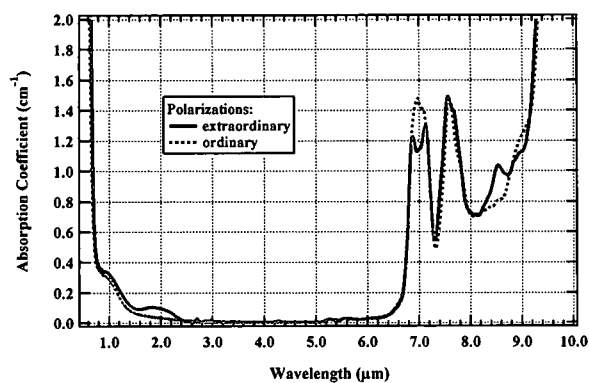


Figure 5.3: Measured absorption spectra for o and e polarized light for CdSiP_2 sample 9A.

5.3 Experimental Layout

The experimental layout is shown in Figure 5.4. A transversely excited atmospheric pressure (TEA) CO₂ laser is used to pump two AgGaSe₂ crystals. Repetition rate of the laser was 4 Hz and the output pulse width is 120 nsec (FWHM). The TEA CO₂ laser is grating tuned to 9.569 μm and the output is linearly polarized with a typical energy of 38 mJ. A 3X down telescope formed by lens pair L1 and L2 loosely focuses the beam into the AgGaSe₂ crystals.

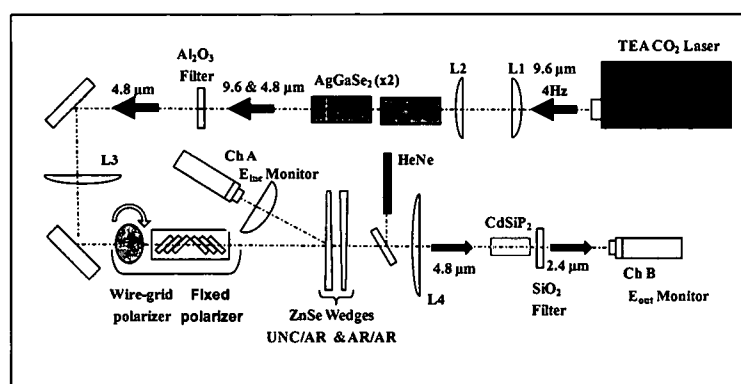


Figure 5.4: Experimental SHG/FHG layout. A TEA CO₂ laser pumps two AgGaSe₂ crystals to generate 4.78 μm light. This is then used as the pump source for second harmonic generation experiments in the CdSiP₂ crystal.

Frequency doubling with tandem AgGaSe₂ crystals produces 10 mJ of energy at 4.78 μm measured after the Al₂O₃ filter. Due to walk-off in the AgGaSe₂ crystals, the 4.78 μm beam is elliptical and slightly astigmatic. The 4.78 μm beam is collimated with lens L3 and sent through a wire grid polarizer. The wire grid polarizer is mounted on a computer controlled rotation stage and in combination with the fixed linear polarizer provides a continuously variable attenuation of over 100:1.

Next, a pair of ZnSe wedges are used for energy monitoring. The first wedge surface is uncoated and sends a portion of the beam to the incident energy monitor (Ch. A). The remaining wedge surfaces are antireflection (AR) coated and used to steer the beam back on-axis. An AR coated lens L4, fl = 15" plano-convex, is used to focus the $4.78\text{ }\mu\text{m}$ beam into the CdSiP₂ crystal. The $4.78\text{ }\mu\text{m}$ beam was vertically polarized with respect to the optical table. Spatial profile of the incident beam was Gaussian and the average beam radius was $128\text{ }\mu\text{m}$ (HW1/eM). The CdSiP₂ crystal was mounted on a computer controlled rotation stage which rotated the crystal parallel to the table. For this experiment the o-polarized pump was vertical and the e-polarized second harmonic was horizontal.

An uncoated piece of SiO₂ was placed after the CdSiP₂ crystal to filter the residual $4.78\text{ }\mu\text{m}$ pump beam. With the CdSiP₂ crystal removed, when 3 mJ of $4.78\text{ }\mu\text{m}$ was incident onto the SiO₂ crystal and no measurable energy (Ch. B < 0.01 μJ detector limit) was observed in the energy detector placed after it. Using a spectrometer, the transmission of the SiO₂ filter at $2.39\text{ }\mu\text{m}$ was measured to be 92.3%, as expected from Fresnel transmission. Results presented below at $2.39\text{ }\mu\text{m}$ account for the transmission loss from the SiO₂ filter.

5.4 SHG Theory and Numerical Model

To compare experimental results with theory, a split step numerical model was used (see Ch. 4). Second harmonic generation in CdSiP₂ at a pump wavelength of $4.79\text{ }\mu\text{m}$ is a Type I process with the pump field (A_P) o-polarized and the signal field (A_S) e-polarized. The set of coupled

differential equations describing the interactions of the A_P and A_S fields inside the crystal are [38]

$$\frac{\partial A_P}{\partial z} = \frac{i}{2k_P} \nabla_{\perp}^2 A_P + \frac{i2d_{\text{eff}}\omega_P}{cn_P} A_P^* A_S \exp(i(k_S - 2k_P)z) - \frac{\alpha_P}{2} A_P \quad (5.3)$$

$$\begin{aligned} \frac{\partial A_S}{\partial z} = & \frac{i}{2k_S} \nabla_{\perp}^2 A_S - \tan(\rho) \frac{\partial A_S}{\partial x} \\ & + \frac{i2d_{\text{eff}}\omega_P}{cn_S} A_P A_P \exp(-i(k_S - 2k_P)z) - \frac{\alpha_S}{2} A_S \end{aligned} \quad (5.4)$$

where walk-off of the signal field is with respect to the x-axis. To numerically model Equations (5.3) and (5.4) the split step method was used by separating the right hand side of the equations into linear and nonlinear operations which are handled separately.

First the crystal length is divided into a number of slices of length Δz . The initial A_P field is known from the experimental conditions and the initial A_S field is zero. Since the sample is uncoated, the A_P field inside the sample is scaled by the Fresnel loss factor. Next, with the nonlinearities turned off, diffraction and walk-off are solved by use of the two dimensional fast Fourier transform beam propagation method [51, 44] (FFT-BPM). Then diffraction and walk-off are set to zero and linear absorption and nonlinear coupling between the fields was solved via a pair of coupled finite difference approximations. First the field equation was solved for A_S to determine A_S after the first step. After solving for the A_S field, the equation for the A_P field was solved. The new A_S and A_P fields were then used as the initial conditions for the next Δz slice. This process is repeated for each Δz step through the crystal. At the exit of the crystal the fields were modified by the transmission coefficients and were temporally and spatially integrated to calculate the output energies.

5.5 Experimental and Theoretical Results

Initially, the CdSiP_2 was placed at the focus of lens L4 with the incident $4.78 \mu\text{m}$ energy low and with the crystal face normal to the pump beam. Using a computer controlled stage to rotate

the crystal, the output energy at $2.39 \mu\text{m}$ was measured as a function of incidence angle. Optimum SHG was found to occur at an incidence angle of 0.26° , in agreement with theory. Figure 5.5 shows the crystal orientation with respect to the pump and signal polarizations and the output energy as a function of incidence angle. The FWHM angular acceptance was found to be 0.77° .

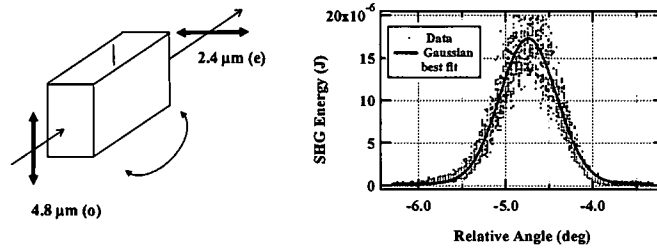


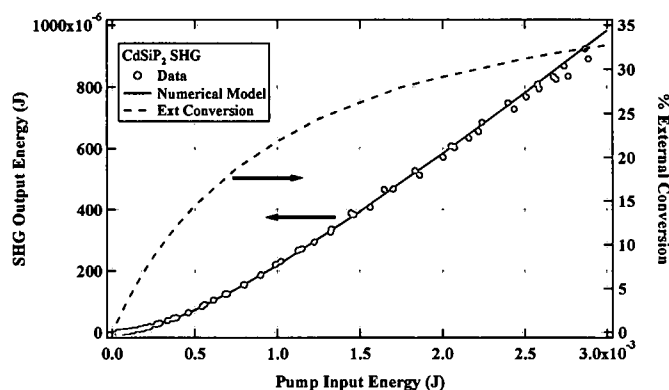
Figure 5.5: Orientation of o and e polarized light in CdSiP_2 and dependence of conversion efficiency on angle of incidence

Next the attenuation was maximized and a data acquisition program was run to record 20 shot averages of the readings on detectors A and B as a function of attenuation. The data was then analyzed and the appropriate calibration factors were applied. A graph showing the output energy and external conversion as a function of incident energy is shown in Fig. 5.6. Table 5.1 summarizes the material parameters used in the model.

In Fig. 5.6, the circles are the average measured energies and the solid red line is the result of numerical modeling of Equations (5.3) and (5.4). Good agreement is found between the model and experimental data with no free parameters used in the model. The d_{eff} value used was 57.6 pm/V as measured by Petrov [52]. The temporal profile of the $4.78 \mu\text{m}$ beam was slightly asymmetric (see Fig. 5.7) and this actual temporal profile was used in the model. The dashed blue line is the external conversion efficiency ($E_{\text{out}}/E_{\text{in}}$). Since the surface damage threshold of CdSiP_2 was unknown,

Table 5.1: CdSiP₂ material parameter values used in modeling of SHG interaction

	ω_{pump}	$2\omega_{\text{pump}}$
Wavelength (μm)	4.78	2.39
Polarization	e	o
$\alpha(\text{cm}^{-1})$	0.001	0.25
d_{eff} (pm/V)	57.6	
$n(e, \theta) = n(o)$	3.0512	
Refl./Surf	25.6%	

Figure 5.6: Second harmonic output energy external conversion efficiency at 2.39 μm as a function of incident pump energy from a CdSiP₂ crystal.

the maximum incident energy was stopped at 3 mJ, or a peak fluence of 5.8 J/cm². Over 30% external conversion was observed at an incident energy of 2.9 mJ. The corresponding peak incident irradiance was 56 MW/cm². Accounting for Fresnel losses at the pump and second harmonic, internal conversion efficiency was 55%. Pump depletion within the crystal was 67%.

Figure 5.7 shows the temporal profiles of the pump and second harmonic at an input energy of 1 mJ. The solid red line is the actual temporal profile of the $4.78\ \mu\text{m}$ beam and is used in the model. The dashed red line is the theoretical on-axis pump pulse at the exit face. The middle, solid blue, line is the theoretical temporal profile of the $2.39\ \mu\text{m}$ at the spatial maximum. Substantial pump depletion is observed at the exit of the sample. The theoretical depleted pump and generated signal temporal traces are in good agreement with observations in the lab.

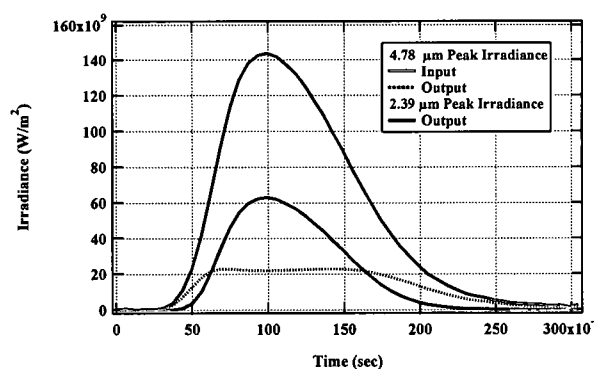


Figure 5.7: Temporal profile of the input $4.78\ \mu\text{m}$ pump beam and the theoretical output of the generated signal and depleted pump beams.

5.5.1 SHG Theoretical Optimization

With the excellent agreement shown in Fig. 5.6 between experiment and numerical modeling, the numerical model was run with different incident pump profiles to determine if there was an optimum pump size that would enhance the SHG conversion. The first numerical experiment was to run the model with different pump radii. A plot of external conversion efficiency as a function of incident pump energy for different pump spot sizes is shown in Fig. 5.8. Material parameters are the

same as in Table 5.1. The solid lines are increasing pump beam radius, r_0 (HW1/eM of irradiance) from 75 to 200 μm . All solid lines end at the same value of fluence/irradiance equivalent to the maximum value in Fig. 5.6. The middle (blue) line is from the experimental results given earlier. The dashed line is a continuation of the $r_0 = 75 \mu\text{m}$ spot size at values that would damage the crystal. The conversion efficiency for all pump beam spot sizes asymptotically approaches the same value, indicating that pump beam depletion is the limiting factor in the conversion efficiency.

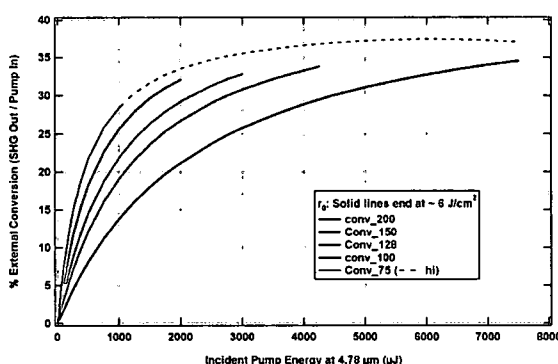


Figure 5.8: SHG conversion efficiency in uncoated CdSiP_2 as a function of incident pump beam spot size. Solid lines end at the same fluence/irradiance value.

In any critically phase matched process, walk off is also a factor in optimization of the conversion efficiency. To investigate its influence, the pump beam was modeled with various elliptical profiles while keeping the same peak irradiance at a constant energy of 3 mJ. The ellipticity was defined as the ratio of r_x/r_y such that for values greater than one, the beam was larger in the walk-off plane, the x-axis for this crystal. Results are shown in Fig. 5.9. While maintaining a constant irradiance and varying the ellipticity from 1 to over 5x, only a 4% enhancement in output energy was observed, indicating again that the optimum conversion has been reached due to pump depletion.

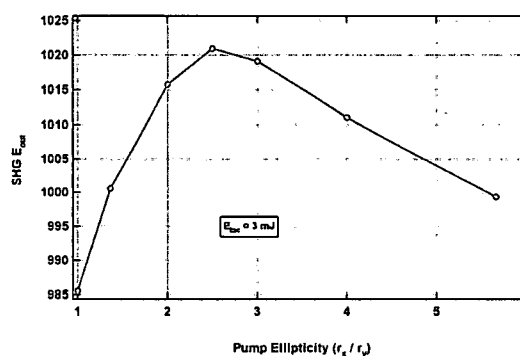


Figure 5.9: SHG output energy in CdSiP₂ as a function of incident pump beam ellipticity. Pump beam radii were chosen such that peak irradiance remained constant at 3 mJ of pump energy. Crystal walk-off is in the x-axis plane.

5.6 Conclusion

The first experimental results of second harmonic generation in CdSiP₂ were obtained. External conversion efficiencies of over 30% were observed at 2.4 μm with approximately 1 mJ of energy in a 100 nsec duration pulse. Excellent agreement was obtained between experimental results and numerical modeling and close to optimal conversion efficiency was observed.

CHAPTER VI

INTRINSIC TWO PHOTON AND FREE CARRIER NONLINEARITIES IN InP

6.1 Introduction

The first part of this chapter discusses results of nonlinear absorption measurements in InP and is based on a paper submitted to the journal Optics Express [8] in which the results obtained at room temperature are presented. Here the cryogenic nonlinear absorption results are also included. The second part of this chapter covers a study of nonlinear refraction measurements in InP, results of which at $1.064\ \mu\text{m}$ have been submitted to the 2009 OSA Nonlinear Optics Conference [7].

Two photon absorption (2PA) is a nonlinear optical phenomenon readily observed with lasers having irradiance in the MW/cm^2 level or above if the photon energy of the laser beam is greater than or equal to half the bandgap of the semiconductor. The 2PA process generates free $e - h$ pairs that modify the linear absorption via free carrier absorption (FCA). In addition, the generated free carriers alter the phase of the beam through nonlinear refraction (NLR).

The strength of the FCA process is determined by the free carrier absorption cross section, σ_{abs} . Free carrier refraction (FCR) coefficient, σ_{ref} , also written as $\frac{dn}{dN}$, relates the change in refractive index to the carrier concentration of the generated charges. The amount of carriers generated is dependent on the pulsewidth and irradiance of the laser source and thus the total NLA and NLR are dependent on the integrated irradiance (fluence) of the incident pulse. For pulse durations in the

range of 10's of ps and longer, FCA and FCR initiated by 2PA are the dominant nonlinear absorption and refraction mechanisms at high values of incident irradiance.

Previously published values of the 2PA coefficient, β , at 1.064 μm varying from 90 to over 200 cm/GW [31, 32]. More recent work at 1.55 μm reports a β between 24 - 33 cm/GW [34]. Theoretical values reported at 1.064 μm also vary from 26 to over 300 cm/GW [35]. No nonlinear measurements of σ_{abs} or σ_{ref} in InP have been reported in the literature.

Through agreement of numerical modeling and experimental results, the nonlinear optical coefficients are extracted in this chapter. Nonlinear absorption measurements were conducted on 0.96 and 2.0 mm thick samples of undoped (*n*-type) InP using the irradiance scan method [4]. Nonlinear measurements were also conducted on a 0.92 mm sample of Fe:InP. Since free carrier absorption in InP is predominately from absorption due to holes, absorption coefficients of two *p*-type InP samples (Zn:InP) were measured as a function of wavelength. Hall measurements on these two samples provided their carrier concentrations, from which the hole absorption cross section at different wavelengths were determined. The values were consistent with earlier measurements [53, 34] but differed from the value obtained from the NLA measurements at 1.535 μm that are presented here.

In addition, a modification of the irradiance scan method was used to analyze NLR in the 0.96 mm intrinsic InP sample. The 2D spatial phases of the ns laser sources incident on the sample were retrieved. In addition the 2D spatial amplitude distributions as well as the temporal profiles of the incident beams were used to model nonlinear propagation through the sample. For determining the FCR coefficient, the beam was allowed to propagate beyond the sample and the beam image was captured with a camera. The σ_{ref} coefficient was determined through analysis of the captured beam images and numerical beam propagation to that plane.

6.2 Theory and Numerical Modeling

As derived in Ch. 3, Eq. (6.1) describes the propagation of a complex electro-magnetic field amplitude, $A(x, y, z, t)$, through a third order nonlinear medium along the z direction in the slowly varying amplitude approximation.

$$\frac{\partial A}{\partial z} = \frac{i}{2k_0} \nabla_{\perp}^2 A + \frac{2i\pi}{\lambda} \left(\sigma_{\text{ref}} N + \frac{dn}{dT} \Delta T + \gamma I \right) A - (\alpha + \sigma_{\text{abs}} N + \beta I) \frac{A}{2} \quad (6.1)$$

where

$$\nabla_{\perp}^2 = \frac{\partial^2}{\partial x^2} + \frac{\partial^2}{\partial y^2} \quad (6.2)$$

In Eq. (6.1), N denotes the density of the generated electrons (and holes) and ΔT is the temperature change brought about by absorption of light. σ_{ref} is the free carrier refraction cross-section (equal to $\frac{dn}{dN}$, the change in refractive index (n) per unit change in carrier density, N), $\frac{dn}{dT}$ is the thermo-optic coefficient and γ denotes the nonlinear refraction coefficient [54]. α is the linear absorption coefficient, σ_{abs} is the total free carrier absorption coefficient and β denotes the 2PA coefficient.

For laser pulses of picosecond and nanosecond duration, diffusion of carrier density and temperature can be ignored and the following equations apply

$$\frac{\partial N}{\partial t} = \frac{\alpha I}{h\nu} + \frac{\beta I^2}{2h\nu} - \frac{N}{\tau} \quad (6.3)$$

$$\frac{\partial \Delta T}{\partial t} = \frac{1}{\rho c} [(\alpha + \sigma_{\text{abs}} N) I + \beta I^2] \quad (6.4)$$

where ρ denotes the density and c denotes the specific heat of the medium. This assumption was verified by measuring the nonlinear transmission using ns lasers at different spot sizes. Experimentally, it was found that the change in transmission as a function of irradiance was not spot size dependent, indicating that carrier diffusion is not significant at these ns pulse durations.

Equation (6.1) is numerically solved via the operator splitting method [45, 55, 30]. The right side of the equation is separated into linear and nonlinear operations which are solved independently. First the sample length is divided into a number of slices of length Δz . At $z = 0$, experimentally determined field is used and is the incident distribution $A(x, y, 0, t)$. Next, with the nonlinearities turned off, Eq. (6.1) is solved over a distance $\frac{\Delta z}{2}$ for each time slice by use of the two dimensional fast Fourier transform beam propagation method [51, 44]. Then diffraction is set to zero and the rate equations (6.3) and (6.4) are solved at this z location via finite difference approximations. The values for $N(x, y, t)$ and $\Delta T(x, y, t)$ are used to modify the electric field. Lastly the field is propagated by a distance $\frac{\Delta z}{2}$ with the nonlinearities set to zero in Eq. (6.1). This process is repeated until the pulse reaches the end of the sample. At the exit of the sample the field is modified by the transmission coefficient and is temporally and spatially integrated to calculate the output energy.

For the ps laser sources, a Gaussian temporal distribution, determined by second harmonic generation autocorrelation, was assumed. For the ns sources the temporal distribution was measured using a fast photodiode and oscilloscope (4 GHz). The pulse shape was normalized and a cubic spline method was used to decrease the number of points while not losing any temporal features. This allowed the actual temporal profile to be used in the model for $A(x, y, z, t)$. For all wavelengths and pulse durations, the actual incident spatial profile was used in the model.

Figure 6.1 shows the theoretical nonlinear transmission in InP at $1.064 \mu\text{m}$ as a function of incident irradiance for different laser pulse durations. Here the spatial profile and pulse duration are assumed to be Gaussian and are characterized by r_0 and t_0 which are the Gaussian HW1/eM of the irradiance incident on the sample and temporal profiles respectively.

The parameters used in Fig. 6.1 are $\beta = 25.5 \text{ cm/GW}$ and $\sigma_{\text{abs}} = 1.54 \times 10^{-17} \text{ cm}^2$. Recombination lifetimes are assumed to be long compared to t_0 . As seen from the graph, for t_0 below

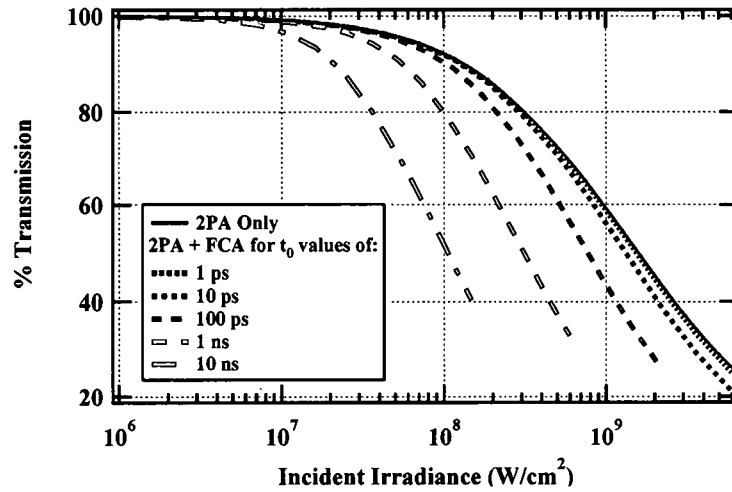


Figure 6.1: Nonlinear absorption in InP at $1.064 \mu\text{m}$ for different pulse durations. As the pulsewidth increases, contributions from free carrier absorption becomes significant.

1 ps free carrier effects can be ignored allowing β to be found directly. However once t_0 begins to exceed ~ 10 ps, free carrier effects can no longer be ignored. Since the lasers used in this work have pulse durations of 10 ps and longer, both β and σ_{abs} are included in the analysis.

6.3 Linear Transmission and Free Carrier Absorption

Transmission spectra of the samples used in the NLA measurements are shown in Fig. 6.2. All three samples had anti-reflection (AR) coatings, the Fe doped sample was coated with a single layer AR film and the undoped samples had broadband AR coatings.

In addition to nonlinear measurements on undoped and Fe doped (n -type) samples, linear measurements on two uncoated, Zn doped (p -type) samples of different carrier concentrations were performed. They were 0.39 and 0.35 mm thick with concentrations (N) of 3.1×10^{-17} and

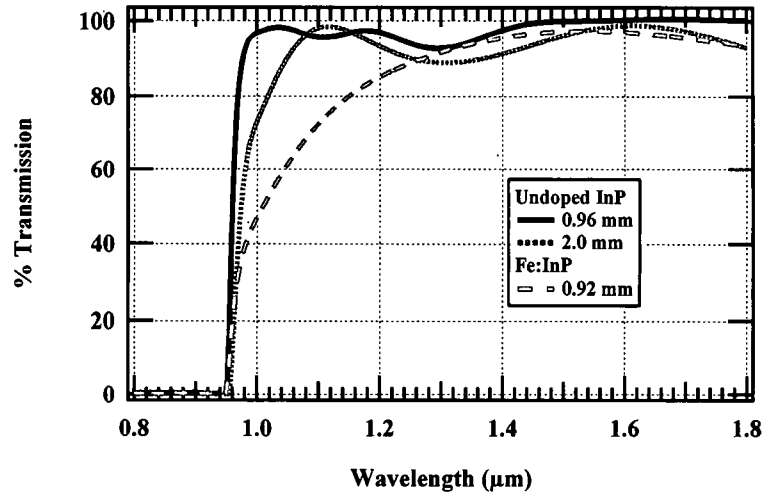


Figure 6.2: Transmission spectra of undoped and Fe doped InP samples used for NLA measurements. Undoped samples have multi-layer AR coatings while the Fe sample has a single layer coating.

$1.9 \times 10^{-18} \text{ cm}^2$ respectively as determined by Hall measurements. The refractive index as a function of wavelength was found using [56]. Linear absorption (α) was determined from the standard etalon transmission expression. Since the samples are *p* type, the free carrier absorption cross section due to holes was determined by $\sigma_h = \alpha/N$.

Figure 6.3 shows the transmission and average σ_h from both Zn doped samples as a function of wavelength. The σ_{abs} values used in the NLA analysis are from contributions of both σ_e and σ_h , although NLA due to holes is the dominant FCA mechanism. The values of σ_h at 1.064 and 1.535 μm found here, as well as in [34] and [53] are shown in Table 6.1

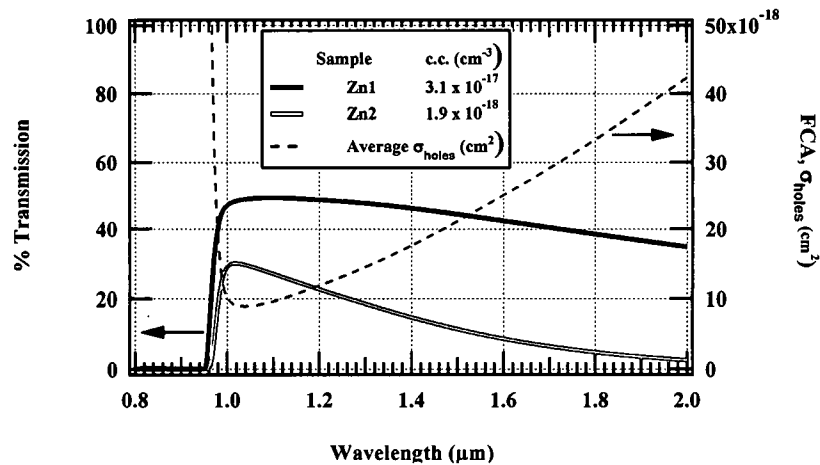


Figure 6.3: Transmission spectra of Zn doped InP samples and average hole free carrier absorption cross section.

Table 6.1: Comparison of $\sigma_h [\times 10^{-17} \text{ cm}^2]$ values at 1.064 and 1.535 μm from linear transmission measurements

$\lambda(\mu\text{m}) =$	1.064 μm	1.535 μm
Fig. 6.3	0.91	2.2
Vignaud [34]	-	1.89
Casey & Carter [53]	0.9 - 2	2 - 3

6.4 Nonlinear Absorption in InP

6.4.1 Experiment and Analysis

A mode locked Nd:YAG laser at 1.064 μm (Ekspla PL2134) provided the ps duration pulses. This laser is also frequency doubled to pump a tunable optical parametric generator providing pulses in the 0.7 to 2.4 μm spectral range (Ekspla PG501). Nanosecond pulse duration measurements were

done with flashlamp pumped, electro-optically Q-switched lasers. A commercial laser was used at $1.064\ \mu\text{m}$ (Quantel Brilliant). Nanosecond measurements at $1.535\ \mu\text{m}$ were done with a laser built in-house with an Er doped phosphate glass laser rod (Kigre, Inc.). Based on the available energy, the beams were loosely focused and the spatial profiles at the beam waists were measured using either a camera or through an xy pinhole scan.

The irradiance scan method [4] was used where the sample was placed at the beam waist and the incident energy was varied, typically through the use of a waveplate and polarizer. A beam splitter was placed prior to the sample and the incident energy was monitored using a pyroelectric energy detector. A second energy detector was placed immediately after the sample in order to capture the total transmitted energy. Significant nonlinear refraction was observed and transmission measurements were verified to ensure that all the transmitted energy was captured. Energy measurements were performed using a ratiometer (LaserProbe, Inc. RM6600 and RJ7620).

Prior to any nonlinear measurements, linearity of the system was verified by ensuring that the ratio of the detectors remained constant over the entire range of attenuation. Care was also taken to ensure that the detectors were not damaged by using neutral density filters as necessary.

The β and σ_{abs} values were obtained by fitting the experimentally determined energy transmission values to those obtained by simultaneously solving Eq. (6.1), (6.3), and (6.4) numerically using different values of the parameters. At each wavelength the upper limit of $\beta(\beta_{\text{max}})$ was found by fitting the data obtained using the ps duration laser with σ_{abs} set equal to zero. The lower limit of $\beta(\beta_{\text{min}})$ was then determined by choosing the minimum value of β for which the ps duration data fitted with the theoretical values obtained with various values of σ_{abs} . For example, at $1.064\ \mu\text{m}$, if β was chosen to be $20\ \text{cm/GW}$ and below, there was no value of sigma for which agreement would be obtained between the theoretical and experimental values. Thus, from picosecond measurements

Table 6.2: Values of β and σ_{abs} at 1.064 and 1.535 μm

$\lambda(\mu\text{m})$	$\beta \left(\frac{\text{cm}}{\text{GW}}\right)$	$\sigma_{\text{abs}} (\text{cm}^2)$
1.064	25.5	1.5×10^{-17}
1.535	14.6	7.2×10^{-17}

at 1.064 μm it was concluded that β was between 20 and 30 cm/GW. At 1.535 μm the range was found to be between 11 and 23 cm/GW.

Analysis of the ns measurements of total transmission showed that the fitting parameter was the product of β and σ_{abs} that provided the best fit to the experimental data. For the 1.064 μm ns data, the $\beta\sigma_{\text{abs}}$ product that provided the best fit to the experimental data was $38 \pm 15\%$. At 1.535 μm the product giving the best fit was found to be $105 \pm 15\%$. Keeping the product constant, the β and σ_{abs} values could be varied by factors of 2 or more yet still gave good agreement to the data. This was not the case for the ps data. Although FCA is present at these ps pulse durations, the dominant absorption mechanism is 2PA with only a slight, but nonzero, FCA contribution.

Using the theoretical values in [36] and the σ_{abs} values from the transmission spectra as starting values, and with bounds on β , both the ns and ps results were iteratively modeled until consistent values were found which fit the data for all the samples at a given wavelength. Recombination lifetimes were assumed to be much longer than the pulse duration for the undoped samples. Good agreement was found for both the 0.96 and 2.0 mm undoped InP samples at both pulse durations and wavelengths. Table 1 summarizes the best fit β and σ_{abs} values. Experimental and numerical modeling results of NLA at 1.064 μm are given in Fig. 6.4 and at 1.535 μm in Fig. 6.5. For clarity, measurements on the Fe:InP sample are not shown in Figs. 6.4 or 6.5. At 1.535 μm , data from the Fe:InP sample is identical to the results from the undoped, 0.96 mm sample. At 1.064 μm the linear

transmissions are different between the samples, but accounting for transmission losses, the same set of β and σ_{abs} coefficients gives good agreement to the data.

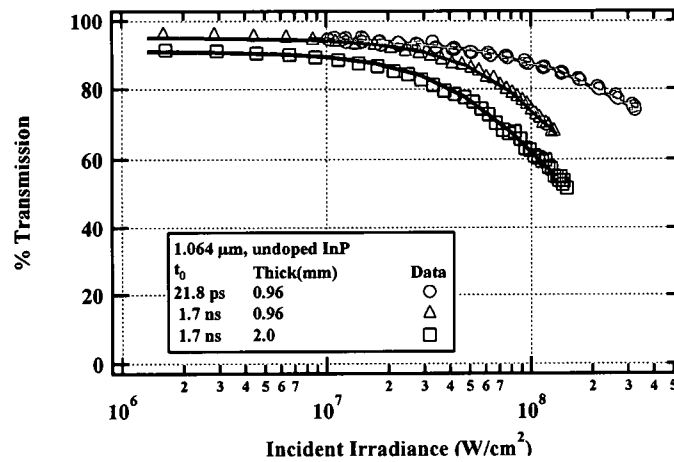


Figure 6.4: Nonlinear absorption results (open symbols) at 1.064 μm on undoped InP samples. Solid lines are theoretical results using values of $\beta = 25.5 \text{ cm/GW}$ and $\sigma_{\text{abs}} = 1.5 \times 10^{-17} \text{ cm}^2$ for all data.

The σ_{abs} value from analysis of the 1.064 μm NLA data is in close agreement with the value determined from linear measurements of the Zn doped samples. At 1.535 μm the value determined from the NLA data is a factor of 3.3 times higher. Note that if the value from the linear transmission measurement is assumed, a β value can be found to fit the ns measurements but will not be in agreement with the ps results. The inverse is also true, if the ps data is analyzed first using σ_{abs} from the linear measurements and finding the best fit β , this $\beta \sigma_{\text{abs}}$ pair will not agree with the ns results. The values given here at the two wavelengths are consistent between both the undoped InP samples at both pulse durations as shown in Fig. 6.5.

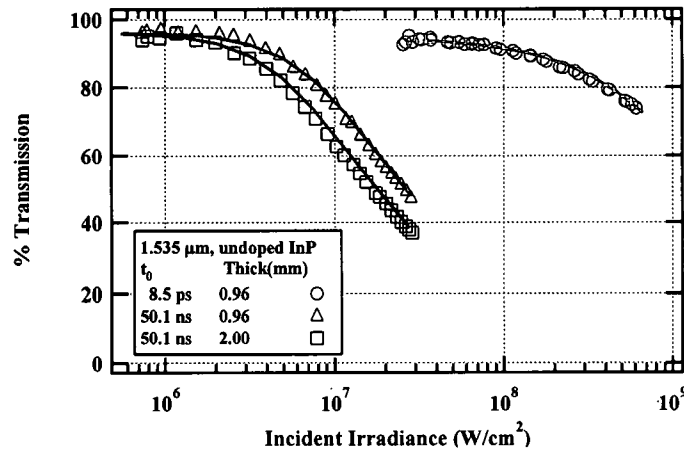


Figure 6.5: Nonlinear absorption results (open symbols) at $1.535 \mu\text{m}$ on undoped InP samples. Solid lines are theoretical results using values of $\beta = 14.6 \text{ cm/GW}$ and $\sigma_{\text{abs}} = 7.2 \times 10^{-17} \text{ cm}^2$ for all data.

Although NLA data between the Fe doped and undoped InP samples were identical for ps duration pulses, a difference was observed at pulse durations in the ns, for which the Fe:InP showed less NLA compared to the undoped sample. The temporal shape of the laser pulse exiting the sample at high irradiances was monitored. The undoped samples showed asymmetry in the output temporal profile due to free carrier generation and absorption during the pulse. For the Fe doped sample, the output pulse closely followed the incident pulse, indicating a recombination lifetime shorter than the ns laser t_0 . Figure 6.6 shows the input and output temporal profiles for the 0.96 mm undoped and the Fe doped InP samples at $1.535 \mu\text{m}$, $t_0 = 50\text{ns}$.

Doping of the samples introduces defect states into the material which allow the generated $e-h$ pairs to recombine more efficiently, resulting in a decreased recombination lifetime. Keeping the same β and σ_{abs} values as in the undoped samples, the value of the decay time τ that best fit the Fe:InP NLA data was $\sim 3 \text{ ns}$. Figure 6.7 shows a comparison of the NLA data at $1.535 \mu\text{m}$,

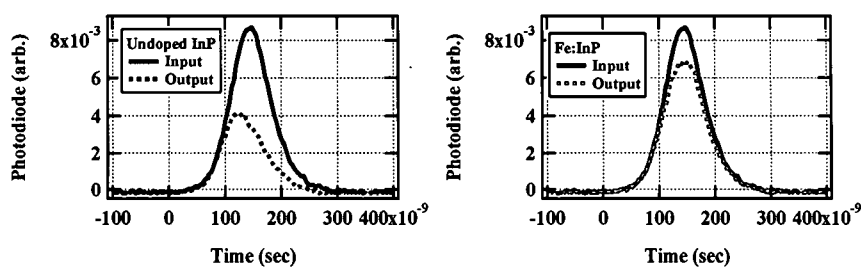


Figure 6.6: Output traces for undoped (left) and Fe doped (right) InP samples at similar incident irradiances. Input wavelength is $1.535 \mu\text{m}$, $t_0 = 50 \text{ ns}$

$t_0 = 50 \text{ ns}$ for undoped and Fe doped InP of similar thicknesses. Nanosecond results at $1.064 \mu\text{m}$ are similar.

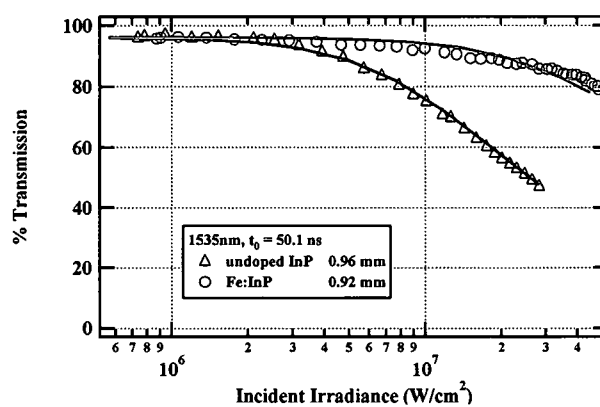


Figure 6.7: Nonlinear absorption in undoped (triangles) and Fe (circles) doped InP at $1.535 \mu\text{m}$, $t_0 = 50 \text{ ns}$. Values of β and σ_{abs} used for both samples are the same. Lifetime in Fe:InP is set to 3 ns and greater than t_0 for the undoped sample.

6.4.2 Results at 77 K

In addition to NLA measurements at 300 K, cryogenic measurements on the 0.96 mm intrinsic InP sample were also performed. As the temperature in InP decreases, the bandgap increases (shorter wavelength), leading to a decrease in β at these wavelengths since they are farther from the bandgap. In addition, at cryogenic temperatures, FCA is expected to decrease [36].

The 0.96 mm intrinsic InP sample was placed within a liquid nitrogen (LN_2) cooled dewar (R. G. Hansen & Assoc.). The front and rear dewar windows were anti-reflection coated CaF_2 substrates. A roughing pump was used to evacuate the dewar and was continuously running while the sample was below room temperature. A temperature sensor at the bottom of the sample holder within the dewar indicated a temperature of 79 K. Nonlinear absorption results of the 0.96 mm undoped InP sample are shown in Fig. 6.8

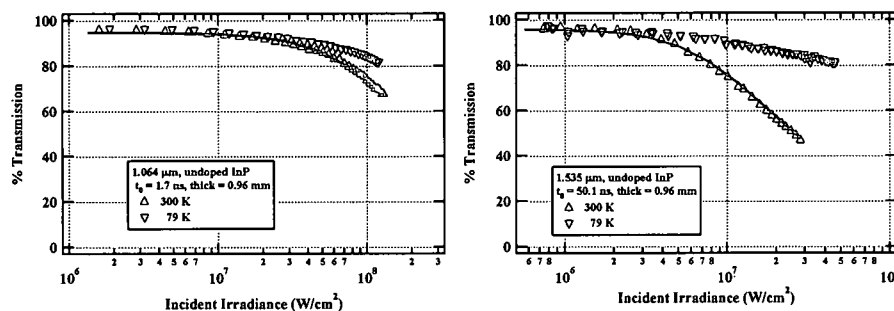


Figure 6.8: Nonlinear absorption in 0.96 mm, undoped InP at room temperature (red) and 79 K (blue). Data was taken at 1.064 (left) and 1.535 (right) μm using the ns lasers. Values of β and σ_{abs} at 79 K are indeterminate.

In neither the 1.064 or 1.535 μm ns NLA data was it possible to find a consistent set of values of β and σ_{abs} which gave good agreement to all the data collected, indicating that further investigation

is required. One possibility is that other physical mechanisms, possibly diffusion, which are not included in the model may have an effect at cryogenic temperatures. However, the measurements showed that at both wavelengths, there is a decrease in NLA, partly due to the bandgap shift with temperature, but predominately due to a decrease in FCA, as seen prominently in the 1.535 μm results. While NLA was less at low temperature at both wavelengths, results at 1.064 μm still showed significant NLA. A possible mechanism that can qualitatively explain the results is enhanced FCA absorption from side valleys in the conduction band (X -valley). Energy levels in these side bands are less sensitive to temperature and the band energy levels are appropriate for NLA at 1.064 μm but not at 1.535 μm .

6.5 Nonlinear Refraction in InP

6.5.1 Theory and Numerical Modeling

For the NLA analysis of the previous section, it was found that only the amplitude distribution was required, the phase information of the input beam was not necessary. NLA modeling with and without the incident phase information typically showed a difference of less than 0.5% in total transmission. In the NLA measurements shown, the beams were collimated through the sample (i.e., sample thickness $\ll Z_R$). If the beams were highly convergent or divergent within the sample this condition may no longer be valid, and for accurate modeling of NLR effects, both the incident amplitude and phase information were required.

To determine the incident spatial amplitude, $A(x, y, z = Z_1, t)$, and phase, $\phi(x, y, z = Z_1)$, the phase retrieval method described in Ch. 4 was used. This was similar to [47] but with the addition of a discrete wavelet transform (DWT). Beam images at two locations, the sample input plane, Z_1 , typically the beam waist, and the detector plane, Z_2 , were recorded. After background corrections,

the square root of each pixel count in the beam images are taken to determine the field amplitudes at each plane. An initial guess is taken for the phase distribution at Z_1 and the complex amplitude is then propagated to Z_2 . The phase and amplitude at Z_2 are separated and the amplitude is replaced with the known amplitude at Z_2 obtained from measurement (square root of pixel counts). A DWT is used on the retrieved phase to filter and smooth the data and minimize noise effects. A complex field at Z_2 based on the original known amplitude and retrieved, filtered phase is back propagated to Z_1 . This process is repeated until the errors are below a preset threshold value.

In the discussion below, the camera position is ideally $\leq Z_R$, but in practice, the minimum distance is driven by physical dimensions of the mechanical hardware involved and the trade off between available energy and spot size to generate sufficient irradiance in order to observe nonlinear effects.

6.5.2 Experimental Results and Analysis

For the previous section which covered NLA measurements, a pyroelectric detector was placed immediately after the sample in order to collect all the transmitted energy. For the NLR measurements, this detector was removed and a pair of wedges were placed after the sample, with the first wedge as close as possible to the sample exit. This first wedge split the beam in two parts. Total transmitted energy was monitored with light transmitted through the wedge. The reflected beam was sent to the second wedge. The two wedges minimized use of neutral density filters and allowed a simple method to align the beam onto the camera.

For NLR measurements using the ns 1.064 μm laser, the distance between planes Z_1 and Z_2 was 650 mm with Z_2 located within the Rayleigh range of the beam. The incident beam was elliptical and approximately Gaussian. Fitting a Gaussian to the beam irradiance gives 1/e radii of 1.0 and

0.5 mm in the horizontal and vertical directions. The effective Rayleigh range for a true Gaussian beam of this waist size is 3 meters. The beam was well collimated between Z_1 and Z_2 , although no attempt was made to determine a beam propagation factor (i.e., M^2) since the 2D amplitude and phase information were used.

Figure 6.9 shows the beam recorded at Z_2 (left) and the result of the numerical model (center) for an incident irradiance of 79 MW/cm^2 . The graph (right) shows a horizontal line profile through the center of both images. The value of σ_{ref} providing the best fit shown is $-3 \times 10^{-20} \text{ cm}^3$. Note that the beam images from the camera and model are not on the same intensity scale since the camera images are background corrected but not calibrated. The object in the lower right portion of the camera image in Fig. 6.9 is due to reflection from the back surface of the wedge closest to the camera.

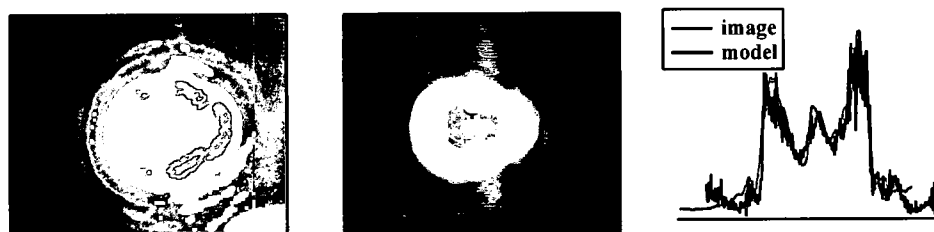


Figure 6.9: Beam image from camera (left) and modeling results (center) at plane Z_2 for an incident irradiance of 79 MW/cm^2 . Graph (right) shows a comparison of the horizontal line profiles through the center of both images.

Similar to Fig. 6.9, Fig. 6.10 shows four comparisons of camera images and numerical results from low irradiance where the sample transmission is linear, 3 MW/cm^2 to higher values of irradiance, 43 MW/cm^2 .

6.6 Conclusion

Nonlinear absorption due to two photon and free carrier effects were investigated in InP. Values for the free carrier absorption coefficient are measured for the first time. A self consistent set of β and σ_{abs} have been determined at 1.064 and $1.535 \text{ }\mu\text{m}$ using undoped samples at 295 K . A decreased recombination lifetime for Fe doped samples was found, which manifests as a decrease in nonlinear absorption for ns laser pulses. The σ_{abs} values obtained through the fitting of modeling result to nonlinear experimental data are about 1.5 and 3.3 times higher than those determined from linear absorption measurements at 1.064 and $1.535 \text{ }\mu\text{m}$ respectively, indicating additional carrier absorption at higher irradiances. Analysis of the cryogenic NLA data using ns laser sources hasn't yielded a consistent set of parameters indicating the need for further analysis.

Nonlinear refraction from free carriers in InP was accurately modeled using known amplitude, phase and temporal profiles of the incident electric field. Good agreement between numerical model and beam images captured after the sample allowed the extraction of nonlinear refraction parameters of InP at 1.064 and $1.535 \text{ }\mu\text{m}$.

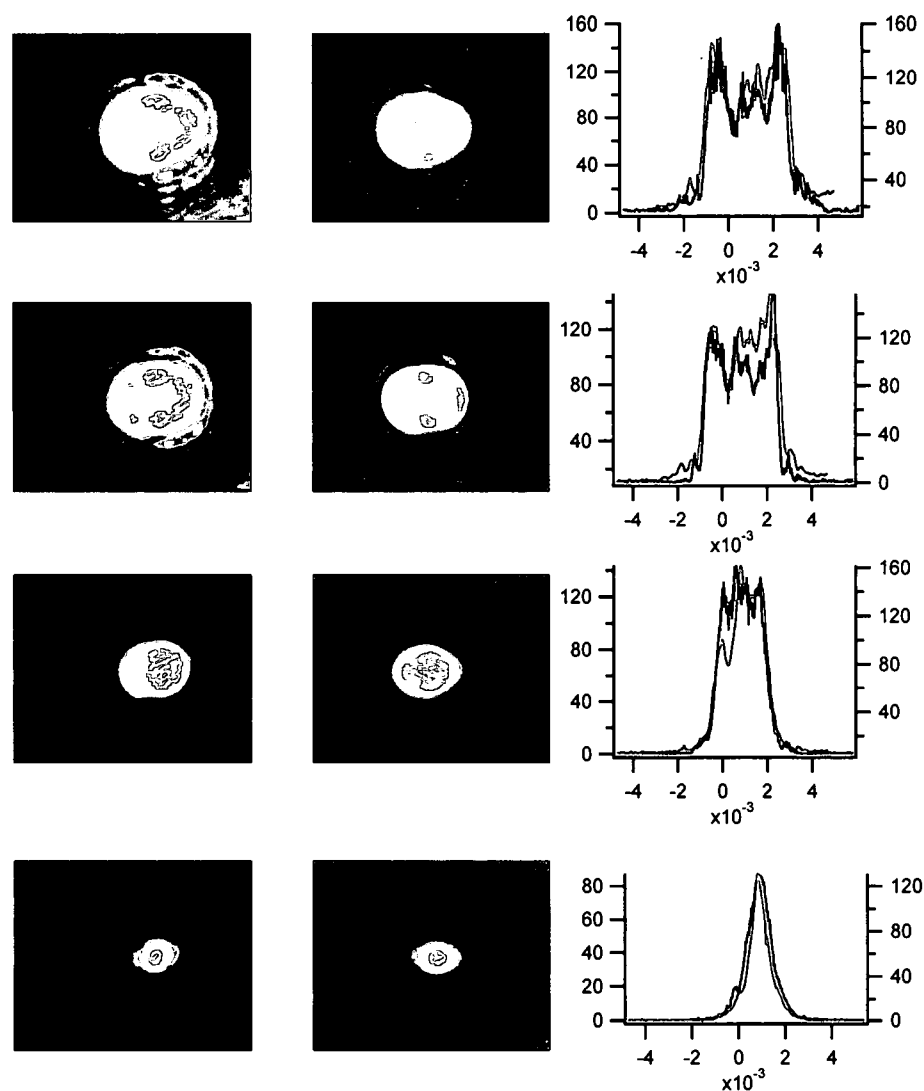


Figure 6.10: Array of beam images from camera (left) and modeling results (center) at plane Z_2 for incident irradiances of 3 (bottom) to 43 MW/cm² (top). Graphs (right) show a comparison of the horizontal line profiles through the center of both images.

CHAPTER VII

CONCLUSION

7.1 Summary

This work has covered investigations of 2nd and 3rd order nonlinearities in semiconductors. A four dimensional numerical model was developed to handle arbitrary spatial amplitude and phase distributions of the field, as well as the actual temporal profile. The first experimental results of second harmonic generation in CdSiP₂ have been presented with external conversion efficiencies of over 30% observed at 2.4 μm with approximately 1 mJ of energy in a 100 nsec duration pulse. Excellent agreement was obtained between experimental results and numerical modeling allowing verification of the material parameters. Close to optimal conversion efficiency was observed, along with substantial pump depletion.

Nonlinear absorption due to two photon and free carrier effects have been investigated in InP. Values for the free carrier absorption coefficient have been measured for the first time. A self consistent set of β and σ_{abs} values have been determined at 1.064 and 1.535 μm using undoped InP samples. A decreased recombination lifetime of the free carriers in Fe doped samples was also observed. Nonlinear refraction was investigated and accurate spatial modeling of the propagated beam was shown.

7.2 Future Work

Potential future work in terms of the numerical modeling is to modify the code to handle other 2nd order nonlinearities such as optical parametric oscillators, both pulsed and continuous wave. For 3rd order nonlinearities, the efficiency of the algorithm could be improved by modifying the step size to be based on an exponential, or adaptive routine. Nonlinear absorption is an irradiance driven process, with the highest irradiance at the entrance to the sample. As the beam propagates through the medium, the irradiance quickly decreases. Having the algorithm use a finer step-size mesh at the beginning of the sample may improve the numerical accuracy. Investigations of longer pulse durations will require inclusion of the diffusion term to the free carrier, and heat, rate equations.

The cryogenic nonlinear absorption and refraction properties of InP require further analysis. Nonlinear absorption and refraction in InP can be further investigated at different wavelengths within the two photon regime. The measurement techniques used here will, and continue to be applied to future samples and the model developed will be especially useful for laser beams of poor quality that arise out of nonlinear generation processes.

The numerical and experimental techniques developed in this work are applicable to a wide range of semiconductor materials over a wide spectrum of wavelengths. Other materials will be studied at different wavelengths of interest.

BIBLIOGRAPHY

- [1] Gonzalez, L., Guha, S., Corbett, M., and Triveldi, S., "Comparison of the nonlinear transmission of $\text{Cd}_{0.65}\text{Mg}_{0.35}\text{Te}$ and CdTe ," in [*Quantum Electronics and Laser Science Conference*], 2, 806–8, OSA (May 2005).
- [2] Krishnamurthy, S., Yu, Z. G., Guha, S., and Gonzalez, L., "High intensity light propagation in InAs," *Appl. Phys. Lett.* **89**, 161108 (3 pgs.) (Oct 2006).
- [3] Krishnamurthy, S., Yu, Z. G., Guha, S., and Gonzalez, L., "Accurate evaluation of nonlinear absorption coefficients in InAs, InSb and HgCdTe alloys," *J. Appl. Phys.* **101**(11), 113104 (2007).
- [4] Gonzalez, L. P., Murray, J. M., Cowan, V. M., and Guha, S., "Measurement of the nonlinear optical properties of semiconductors using the Irradiance Scan technique," *Nonlinear Frequency Generation and Conversion: Materials, Devices, and Applications VII* **6875**(1), 68750R, SPIE (2008).
- [5] Gonzalez, L. P., Guha, S., and Sheng, Q., "Propagation of high intensity light in semiconductors," *PAMM* **7**(1), 1041203–1041204 (2007).
- [6] Gonzalez, L. P., Upchurch, D., Barnes, J. O., Schunemann, P. G., Zawilski, K. T., and Guha, S., "Second Harmonic Generation in CdSiP_2 ," in [*Nonlinear Frequency Generation and Conversion: Materials, Devices, and Applications VIII*], Powers, P. E., ed., **7197**(1), 71970N, SPIE, San Jose, CA, USA (2009).
- [7] Gonzalez, L. P., Guha, S., and Krishnamurthy, S., "Experimental determination of nonlinear absorption and refraction coefficients of InP through accurate spatial and temporal modeling of nanosecond duration laser beams," OSA Nonlinear Optics Conf. (submitted 2009).
- [8] Gonzalez, Leonel, P., Murray, J. M., Krishnamurthy, S., and Guha, S., "Wavelength dependence of intrinsic and free carrier nonlinear absorption in InP," *Opt. Express* (submitted 2009).
- [9] Pino, R., Ko, Y., Dutta, P. S., Guha, S., and Gonzalez, L., "Burstein-moss shift in impurity-compensated bulk $\text{Ga}_{1-x}\text{In}_x\text{Sb}$ substrates," *J. Appl. Phys.* **96**(9), 5349–52 (2004).
- [10] Chandola, A., Kim, H. J., Dutta, P. S., Guha, S., Gonzalez, L., and Kumar, V., "Below band-gap optical absorption in $\text{Ga}_x\text{In}_{1-x}\text{Sb}$ alloys," *J. Appl. Phys.* **98**(9), 093103–7 (2005).

- [11] Dubinskii, M., Merkle, L. D., Goff, J. R., Quarles, G. J., Castillo, V. K., Schepler, K. L., Zelmon, D., Guha, S., Gonzalez, L. P., Rickey, M. R., Lee, J. J., Hegde, S. M., Dumm, J. Q., Messing, G. L., and Lee, S.-H., "Processing technology, laser, optical and thermal properties of ceramic laser gain materials," in [*Laser Source and System Technology for Defense and Security*], Wood, G. L., ed., **5792**, 1–9, SPIE, Orlando, FL, USA (2005).
- [12] Zelmon, D. E., Schepler, K. L., Guha, S., Rush, D. J., Hegde, S. M., Gonzalez, L. P., and Lee, J., "Optical properties of nd-doped ceramic yttrium aluminum garnet," in [*Laser-Induced Damage in Optical Materials: 2004*], Exarhos, G. J., Guenther, A. H., Kaiser, N., Lewis, K. L., Soileau, M. J., and Stolz, C. J., eds., **5647**, 255–264, SPIE, Boulder, CO, USA (2005).
TY - CONF.
- [13] Metcalf, P. A., Guha, S., Gonzalez, L. P., Barnes, J. O., Slamovich, E. B., and Honig, J. M., "Electrical, structural, and optical properties of cr-doped and non-stoichiometric V_2O_3 thin films," *Thin Solid Films* **515**(7-8), 3421–3425 (2007).
- [14] Heckman, E. M., Gonzalez, L. P., and Guha, S., "Measurement of optical and thermal properties of $hg_{1-x}cd_xte$," *Appl. Opt.* **47**(4), 578–582 (2008).
- [15] Guha, S. and Gonzalez, L. P., "Theory of second harmonic generation in presence of diffraction, beam walk-off, and pump depletion," in [*Nonlinear Frequency Generation and Conversion: Materials, Devices, and Applications VI*], Powers, P. E., ed., **6455**, 64550W–10, SPIE, San Jose, CA, USA (2007).
- [16] Guha, S., Gonzalez, L. P., and Sheng, Q., "Description of light focusing by a spherical lens using diffraction integral method," *Proc. Appl. Math. Mech.* **7**(1), 1023301–1023302 (2007).
- [17] Gonzalez, L., Guha, S., Rogers, J. W., and Sheng, Q., "An effective z-stretching method for paraxial light beam propagation simulations," *Journal of Computational Physics* **227**, 7264–78 (2008).
- [18] Gonzalez, L., Guha, S., and Trivedi, S., "Damage thresholds and nonlinear optical performance of GaP," in [*CLEO*], OSA, San Francisco, CA (2004).
- [19] Cowan, V. M., *Characterization of Temperature Dependent Nonlinear Optical Properties of Semiconductor Materials*, M.S. Electro-Optics, University of Dayton, Dayton, OH (2008).
- [20] Corbett, M., *Nonlinear optical properties of indium arsenide with ultrafast femtosecond radiation at mid-infrared wavelengths*, Ph.D. Physics, University of St. Andrews (March 2005).
- [21] Weber, M. J., [*Optical Materials: Part I*], vol. 3 of *Handbook of Laser Science and Technology*, CRC Press, Inc. (1986).
- [22] Braunstein, R., "Nonlinear optical effects," *Phys. Rev.* **125**, 475–7 (1962).

- [23] Braunstein, R. and Ockman, N., "Optical double-photon absorption in CdS," *Phys. Rev.* **134**, A499 (1964).
- [24] VanStryland, E. W., Vanherzeele, H., Soileau, M. J., Smirl, A. L., Guha, S., and Boggess, T. F., "Two photon asorption, nonlinear refraction, and optical limiting in semiconductors," *Opt. Engr.* **24**(4), 613–23 (1985).
- [25] Sheik-Bahae, M., Said, A. A., and VanStryland, E. W., "High-sensitivity, single-beam n_2 measurements," *Opt. Lett.* **14**(17), 955–7 (1989).
- [26] Sheik-Bahae, M., Said, A. A., Wei, T. H., Hagan, D. J., and VanStryland, E. W., "Sensitive measurements of optical nonlinearities using a single beam," *IEEE J. Quantum Electron.* **26**(4), 760–9 (1990).
- [27] Sheik-Bahae, M., Hutchings, D. C., Hagan, D. J., and VanStryland, E. W., "Dispersion of Bound Electronic Nonlinear Refraction in Solids," *IEEE J. Quantum Electron.* **27**, 1296–1309 (June 1991).
- [28] Berryman, K. W. and Rella, C. W., "Nonlinear absorption in indium arsenide," *Phys. Rev. B* **55**(11), 7148–54 (1997).
- [29] Poole, C. D. and Garmire, E., "Nonlinear refraction at the absorption edge in InAs," *Opt. Lett.* **9**(8), 356–8 (1984).
- [30] Haeri, M. B., Kingham, S. R., and Milsom, P. K., "Nonlinear absorption and refraction in indium arsenide," *J. Appl. Phys.* **99**, 013514 – 19 (2006).
- [31] Lee, C. C. and Fan, H. Y., "Two-photon absorption with exciton effect for degenerate valence bands," *Phys. Rev. B* **9**(8), 3502 (1974).
- [32] Dvorak, M. D. and Justus, B. L., "Z-scan studies of nonlinear absorption and refraction in bulk, undoped InP," *Opt. Comm.* **114**(1-2), 147–150 (1995).
- [33] Tiedje, H. F., Haugen, H. K., and Preston, J. S., "Measurement of nonlinear absorption coefficients in GaAs, InP and Si by an optical pump THz probe technique," *Opt. Comm.* **274**(1), 187–197 (2007).
- [34] Vignaud, D., Lampin, J. F., and Molloy, F., "Two-photon absorption in InP substrates in the 1.55 μm range," *Appl. Phys. Lett.* **85**(2), 239–241 (2004).
- [35] Nathan, V., Guenther, A. H., and Mitra, S. S., "Review of multiphoton absorption in crystalline solids," *J. Opt. Soc. Amer. B* **2**(2), 294–316 (1985).
- [36] Krishnamurthy, S., "Nonlinear absorption in InP." preprint (2009).

- [37] Taheri, B., Liu, H., Jassemnejad, B., Appling, D., Powell, R. C., and Song, J. J., "Intensity scan and two photon absorption and nonlinear refraction of C_{60} in toluene," *Appl. Phys. Lett.* **68**(10), 1317–1319 (1996).
- [38] Sutherland, R. L., [*Handbook of Nonlinear Optics*], Optical Engineering, Marcel Dekker, Inc., New York, 1st ed. (1996).
- [39] Moss, T. S., [*Optical Properties of Semiconductors*], Buttersworth Scientific Publications, London (1959).
- [40] Storeboe, A. K., Brudevoll, T., and Stenersen, K., "Calculated temperature rise in midinfrared laser irradiated $Hg_{0.72}Cd_{0.28}Te$," *J. Appl. Phys.* **103**(5), 053108 (2008).
- [41] Sheldon, S. J., Knight, L. V., and Thorne, J. M., "Laser-induced thermal lens effect: a new theoretical model," *Appl. Opt.* **21**(9), 1663–69 (1982).
- [42] Yates, M., Tsangaris, C., Kinsler, P., and New, G., "Modelling of angular effects in nonlinear optical processes," *Opt. Comm.* **257**(1), 164–175 (2006).
- [43] Goodman, J. W., [*Introduction to Fourier Optics*], Roberts & Company, Greenwood Village, CO, 3rd ed. (2005).
- [44] Agrawal, G. P., [*Nonlinear Fiber Optics*], Academic Press, New York, 4th ed. (2007).
- [45] Hughes, S., Burzler, J., Spruce, G., and Wherrett, B. S., "Fast Fourier transform techniques for efficient simulation of Z-scan measurements," *J. Opt. Soc. Amer. B* **12**(10), 1888–93 (1995).
- [46] Gerchberg, R. W. and Saxton, W. O., "A practical algorithm for the determination of phase from image and diffraction plane pictures," *Optik (Stuttgart)* **35**, 237–46 (1972).
- [47] Pandey, A. R., Haus, J. W., Powers, P. E., and Yaney, P. P., "Optical field measurements for accurate modeling of nonlinear parametric interactions," *J. Opt. Soc. Amer. B* **26**(2), 218–227 (2009).
- [48] Ivanov, V. Y., Sivokon, V. P., and Vorontsov, M. A., "Phase retrieval from a set of intensity measurements: theory and experiment," *J. Opt. Soc. Amer. A* **9**(9), 1515 (1992).
- [49] Matsuoka, S. and Yamakawa, K., "Wave-front measurements of terawatt-class ultrashort laser pulses by the fresnel phase-retrieval method," *J. Opt. Soc. Amer. B* **17**(4), 663–667 (2000).
- [50] Schunemann, P. G., Zawilski, K. T., Pollak, T. M., Zelmon, D. E., Fernilius, N. C., and Hopkins, F. K., "New mid-ir nonlinear optical crystal: $CdSiP_2$," in [*Conference on Lasers and Electro-Optics/Quantum Electronics and Laser Science Conference and Photonic Applications Systems Technologies*], *OSA Technical Digest (CD)*, CFX7, Optical Society of America (2008).

R702035247

- [51] Feit, M. D. and Fleck, J. A., J., "Light propagation in graded-index optical fibers," *Appl. Opt.* **17**(24), 3990 (1978).
- [52] Petrov, V. P., Noack, F., Tunchev, I., Schunemann, P. G., and Zawilski, K., "The nonlinear coefficient d_{36} of CdSiP_2 ," in [*Nonlinear Frequency Generation and Conversion: Materials, Devices, and Applications VIII*], Powers, P. E., ed., **7197**(1), 71970M, SPIE, San Jose, CA, USA (2009).
- [53] H. C. Casey, J. and Carter, P. L., "Variation of intervalence band absorption with hole concentration in p-type InP," *Appl. Phys. Lett.* **44**(1), 82–83 (1984).
- [54] Said, A. A., Sheik-Bahae, M., Wei, T. H., Young, J., and Van Stryland, E. W., "Determination of bound-electronic and free-carrier nonlinearities in ZnSe, GaAs, CdTe, and ZnTe," *J. Opt. Soc. Amer. B* **9**(3), 405–14 (1992).
- [55] Kovsh, D. I., Yang, S., Hagan, D. J., and Van Stryland, E. W., "Nonlinear optical beam propagation for optical limiting," *Appl. Opt.* **38**(24), 5168–80 (1999).
- [56] Pettit, G. D. and Turner, W. J., "Refractive index of InP," *J. Appl. Phys.* **36**(6) (1965).